bioRxiv preprint doi: https://doi.org/10.1101/2022.08.16.504030; this version posted August 17, 2022. The copyright holder for this preprint (which was not certified by peer review) is the author/funder, who has granted bioRxiv a license to display the preprint in perpetuity. It is made available under aCC-BY-NC 4.0 International license.

Centripetal integration of past events by hippocampal astrocytes

Peter Rupprecht[1,*], Christopher M Lewis[1], Fritjof Helmchen[1,2,*]

[1] Laboratory of Neural Circuit Dynamics, Brain Research Institute, University of Zurich, Switzerland
[2] Neuroscience Center Zurich, University of Zurich, Switzerland

* Corresponding authors: rupprecht@hifo.uzh.ch, helmchen@hifo.uzh.ch

Abstract

An essential feature of neurons is their ability to centrally integrate information from their dendrites. The activity of astrocytes, on the other hand, has been described to be mostly uncoordinated across the cellular compartments and therefore without central integration. Here, we describe *conditional centripetal integration*, a principle how astrocytes integrate calcium signals from their distal processes. We performed calcium imaging of hippocampal astrocytes and neurons in head-fixed mice, together with monitoring of body movements and pupil diameter. Global astrocytic activity was well explained by the concurrent pupil diameter as a proxy for arousal, but equally well as leaky integration of past neuronal and behavioral events on a timescale of seconds. This integration of past events occurred in a centripetal pattern in individual astrocytes, starting in distal processes followed by a slow propagation towards the soma. Centripetal propagation was facilitated by high levels of arousal but impeded when pre-event calcium levels were high. Together, our results establish astrocytes as computational units of the brain that slowly and conditionally integrate information about the past.

Introduction

Astrocytes have long been thought to play a supportive rather than computational role in the brain. This picture started to change when the close interaction of astrocytic processes and neuronal synapses was discovered, leading to the concept of the tripartite synapse[1,2]. More recent studies have begun to establish a role for astrocytes, as for neurons, in diverse computational processes of the brain[3,4]. For example, calcium signals in astrocytes have been suggested to represent sensory or internally generated information[5–8]. In contrast to neurons, however, information processing in single astrocytes is thought to rely on distributed and mostly uncoordinated activity patterns across the compartments of a single astrocyte, without central integration[9–11]. It is therefore not clear whether and how astrocytes integrate signals that are sensed by their distributed compartments.

The study of signal integration in astrocytes is particularly challenging since they express a large set of receptors that enable them to sense the direct and indirect effects of both neuronal activity and neuromodulatory signals[9,12,13]. Recent work from systems neuroscience has demonstrated that spontaneous behaviors and motor activity drive a large fraction of the variability of neuronal activity in the mouse cortex[14,15]. These studies highlight the importance of a systematic investigation of

bioRxiv preprint doi: https://doi.org/10.1101/2022.08.16.504030; this version posted August 17, 2022. The copyright holder for this preprint (which was not certified by peer review) is the author/funder, who has granted bioRxiv a license to display the preprint in perpetuity. It is made available under aCC-BY-NC 4.0 International license.

possibly interdependent observables in the brain to understand potential confounds between task-related behaviors, spontaneous behaviors, cellular activity patterns, and brain states. In order to understand signal integration in astrocytes, it is therefore essential to study astrocytic activity together with factors that have been shown to influence astrocytic activity, *e.g.,* neuromodulatory signals[8,16,17], locomotion[17–20], and neuronal activity[7,10,11,21,22]. Moreover, it is crucial to carefully analyze how astrocytes may integrate information from these factors, both temporally, in a population of astrocytes, and spatially, within individual astrocytes.

Here, we perform a systematic exploration of astrocytic activity in the hippocampal subregion CA1 in mice using two-photon calcium imaging of astrocyte populations. At the same time, we monitor motor behaviors, track the pupil diameter as a proxy of noradrenergic tone and arousal, and use calcium imaging to observe neuronal activity. This systematic approach enables us to model astrocytic activity using these other variables. Specifically, we describe global astrocytic activity across the hippocampal population as a temporal integration of past salient events. Furthermore, we observe a spatial propagation of calcium signals in astrocytes from distal to somatic compartments that depends on the state of the animal and the state of the astrocytes. Together, our observations reveal a novel principle of spatiotemporal integration of past events within astrocytes in the awake, behaving animal.

Results

A global astrocytic activity mode during behavior

To record astrocytic activity in the hippocampus across a wide range of behaviors, we virally induced expression of GCaMP6s (n = 6 mice; AAV9-GFAP-GCaMP6s; Methods) and performed two-photon calcium imaging in head-fixed mice that were free to run on a treadmill and received water rewards at a defined location of the treadmill, resulting in variable behavior including periods of active running and quiet wakefulness (Fig. 1a). First, we analyzed calcium transients in the astrocyte population using a single imaging plane in *stratum oriens* of CA1 (Fig. 1b-e; Fig. S1; Movie 1). Astrocytic calcium signals were highly correlated across active regions of interest (ROIs, as defined in Methods; Fig. 1f-i), with relatively few prominent local events (Fig. 1f, white arrows). Therefore, the global astrocytic activity, which we define as the average fluorescence trace across the population of astrocytes in the entire field of view (FOV), explained a large fraction of the variance of single astrocyte activity (Fig. 1h,i; correlation: 0.72 ± 0.20, median ± s.d. across 204,686 pairs of astrocytes from 41 imaging session from $n = 6$ mice). The correlation of activity only decayed slightly with the distance between astrocyte pairs (Fig. 1j), indicating a global rather than local synchronization within hippocampal CA1. In addition, we observed local events in single astrocytes independent of global activity (white arrows in Fig. 1f) and local modulations of global activity in single astrocytic ROIs (black arrows in Fig. 1g; Movie 1). However, the overall spontaneous activity during behavior was dominated by a global mode across astrocytes.

Global astrocytic activity across hippocampal layers

To understand how astrocytic activity was correlated across different depths of hippocampal CA1, we performed triple-layer calcium imaging using fast z-scanning with a tunable lens[23]. With this approach, we were able to image quasi-simultaneously from astrocytes in the *stratum*

bioRxiv preprint doi: https://doi.org/10.1101/2022.08.16.504030; this version posted August 17, 2022. The copyright holder for this preprint (which was not certified by peer review) is the author/funder, who has granted bioRxiv a license to display the preprint in perpetuity. It is made available under aCC-BY-NC 4.0 International license.

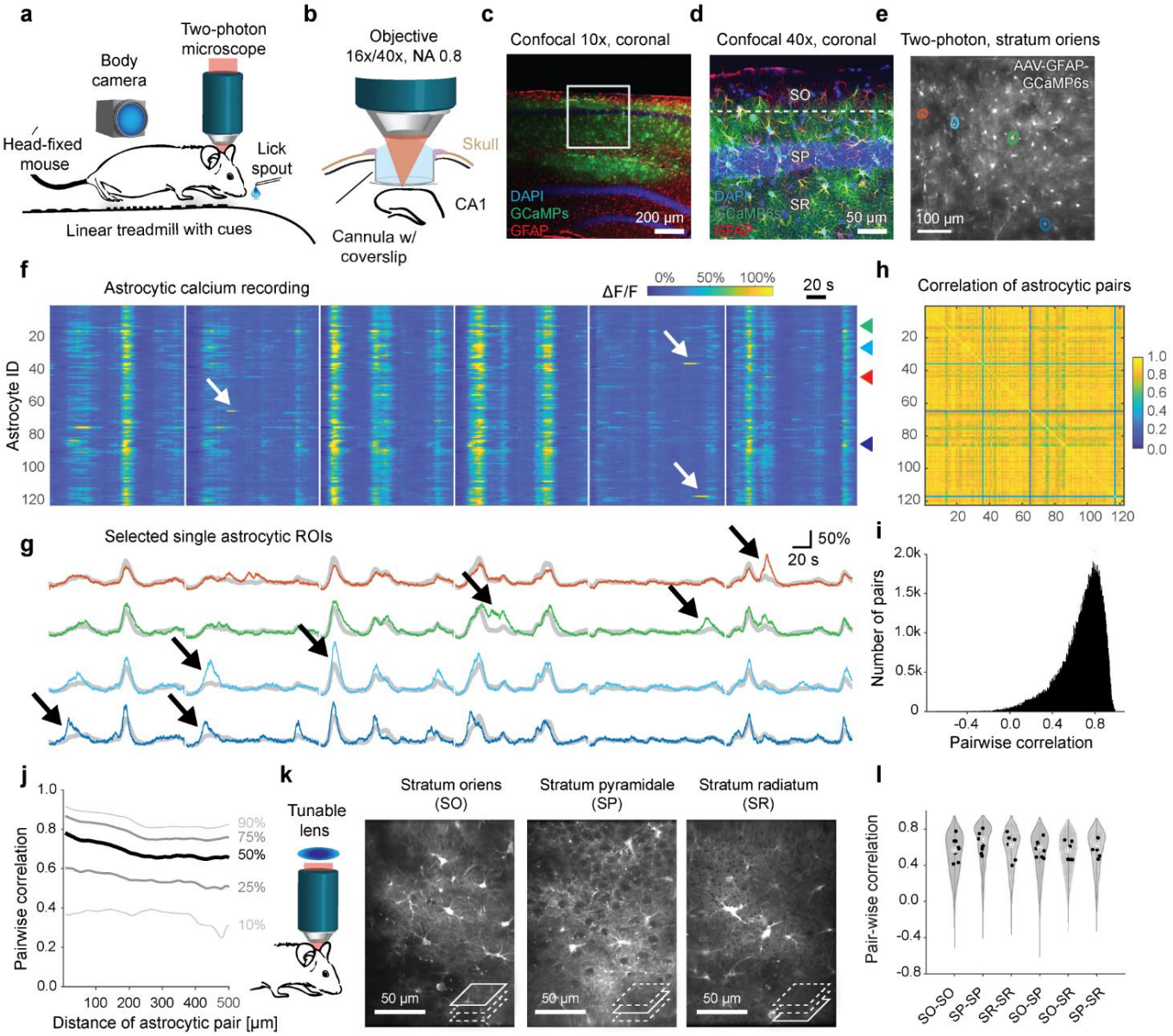

Figure 1 | Hippocampal astrocytes in CA1 exhibit global and local events during behavior. a, Scheme of the *in vivo* recording setup. **b,** Hippocampal two-photon imaging through an implanted cannula. **c-d,** Histology of virus-induced GCaMP6s expression in hippocampal astrocytes (green) together with GFAP-antibody staining (red) and nuclear stain (blue). See also Fig. S1. **e,** Average fluorescence two-photon image of astrocytes in the *stratum oriens* expressing GCaMP6s. **f,** Temporal calcium dynamics of active astrocyte ROIs from the FOV shown in panel (e). White arrows indicate isolated local calcium events. Recording segments (140 s) are indicated through vertical white spacers. **g**, Example of four astrocytic ROIs (highlighted with matching colors in (e) and in (f) with arrow heads), indicating local modulation of global events for astrocytic ROIs (black arrows). Global mean across the FOV is overlaid as grey traces. **h,** Activity correlation between the astrocytic pairs from panel (f), same ordering of ROIs. **i,** Distribution of activity correlations between astrocytic active region pairs across the entire population (204,686 astrocyte ROI pairs from 41 experimental sessions and 6 animals; 0.72 ± 0.20, median ± s.d.). **j,** Distance-dependence of pairwise correlations, with the median (50%) and other percentile lines of the distribution shown. **k,** Using a tunable lens to quasi-simultaneously image multiple CA1 layers. **l,** Pairwise correlation across simultaneously imaged astrocyte pairs associated with specific CA1 layers (distributions in the violin plots), and medians across astrocyte pairs for each session (black dots). No significant differences ($p > 0.2$ for all comparisons) across conditions for session-based testing (n = 8 sessions from 2 animals). ROI, region of interest; FOV, field of view; SO, *stratum oriens*; SP, *stratum pyramidale*; SR, *stratum radiatum*.

bioRxiv preprint doi: https://doi.org/10.1101/2022.08.16.504030; this version posted August 17, 2022. The copyright holder for this preprint (which was not certified by peer review) is the author/funder, who has granted bioRxiv a license to display the preprint in perpetuity. It is made available under aCC-BY-NC 4.0 International license.

oriens, the *stratum pyramidale* and the *stratum radiatum* (Fig. 1k; Movie 2). Astrocytic activity was highly correlated across layers (Fig. 1l) and we did not find evidence that astrocytic pairs were less correlated across layers than within layers ($p > 0.2$ for all comparisons, Wilcoxon's rank sum test, $n = 8$ sessions from 2 animals, with 4,738 to 10,432 astrocytic ROI pairs for each comparison). Due to the sparse occurrence of astrocytic somata in the *stratum pyramidale*[24] and the better imaging access to *stratum oriens*, we focus all the remaining analyses and experiments, unless otherwise stated, on the *stratum oriens* layer of hippocampal CA1.

Astrocytic activity recorded together with neuronal activity, motor behaviors, and pupil diameter

To probe how astrocytic activity relates to the animals' behavior and hippocampal neuronal activity, we performed simultaneous calcium imaging of astrocytes in *stratum oriens* (SO) of CA1 (viral expression of GCaMP6s as before) and of neurons (transgenic Thy1-GCaMP6f background, ref. [25]) in the *stratum pyramidale* (SP) 60-90 µm below the SO-imaging plane (Fig. 2a-c; $n = 4$ mice, 22 imaging sessions). GCaMP signals from astrocytes and neurons were clearly distinct from each other due to their different location (SO vs. SP) and dynamics (slow vs. fast transients), enabling unmixing of neuronal signals through gliapil decontamination (Methods for details). To quantify average neuronal population activity, we extracted $\Delta F/F$ traces from ROIs of neuronal somata, denoised these traces using a supervised deconvolution algorithm based on deep networks[26], and averaged across the denoised spike rates, resulting in an overall hippocampal spike rate (SR) estimate. In addition to calcium imaging, we recorded the animals' run speed as well as the spatial location on the treadmill. Moreover, we used a video camera to record body movements (Fig. 2d). We estimated the movement of the mouth and the paws using the across-frames correlation in corresponding subareas of the videos to calculate movement strengths, and we quantified licking by detecting the tongue from the behavior videos. Finally, we used a dim focused UV light to constrict the pupil in the otherwise dark environment, which allowed us to record pupil diameter as a proxy for neuromodulatory tone and arousal[27–29]. These multiple perspectives (Fig. 2e; Movie 3) enable a comprehensive analysis of astrocytic activity in the context of diverse, possibly related processes and events.

Global astrocytic activity can be explained by pupil diameter, body movement or neuronal activity

Due to the slow changes of global astrocytic activity over time (Fig. 1f,g; Fig. 2e), a typical 15-35 min recording only sparsely samples the state space of astrocytic activity. To understand and explain astrocytic activity, we therefore aimed, in a first step, to explain the global mode of astrocytic activity by either run speed, body movements, pupil diameter or mean neuronal spike rate using simple linear models. In a first approximation, we estimated the shared information between global astrocytic activity and these factors using instantaneous correlation (Fig. 3a). Interestingly, we found that pupil diameter displayed the highest correlation with the global astrocytic signal, whereas run speed, body movements and neuronal activity were less correlated (Fig. 3c).

Next, to account for possible delayed effects that cannot be captured by correlation or other instantaneous measures, we used past and future time points of neuronal and behavioral variables to explain the current value of global astrocytic activity using multi-timepoint, "dilated" linear

bioRxiv preprint doi: https://doi.org/10.1101/2022.08.16.504030; this version posted August 17, 2022. The copyright holder for this preprint (which was not certified by peer review) is the author/funder, who has granted bioRxiv a license to display the preprint in perpetuity. It is made available under aCC-BY-NC 4.0 International license.

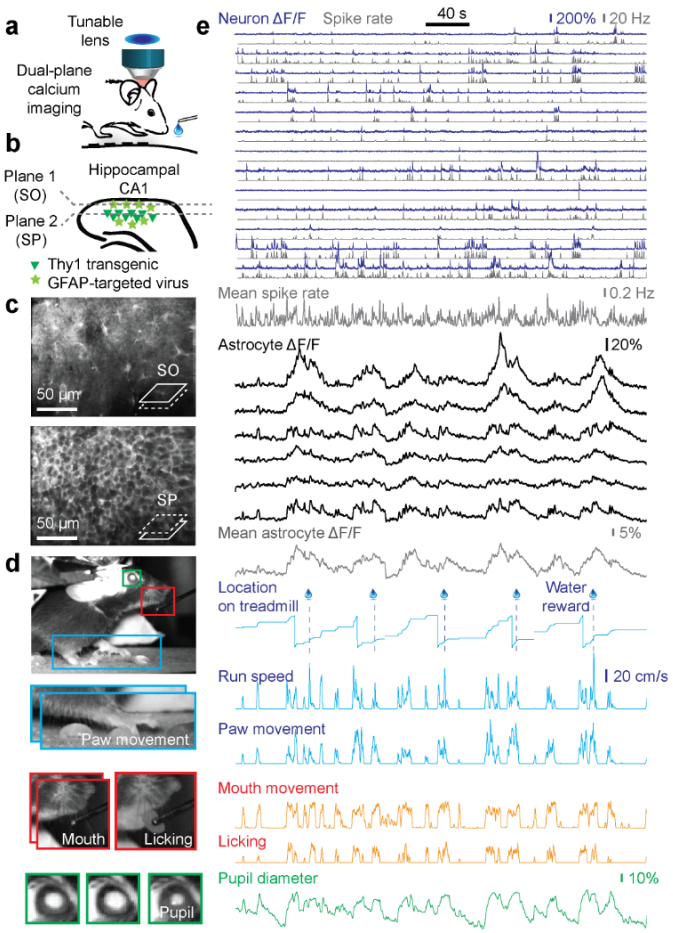

Figure 2. Simultaneous monitoring of astrocytic and neuronal population activity, pupil diameter and behavior. a, Dual-plane calcium imaging using a tunable lens. **b,** Simultaneously imaging of spatially separated astrocytes (*stratum oriens* (SO) layer, virally induced GCaMP6s; star symbols) and transgenically expressed neurons (stratum pyramidale (SP) layer, Thy1-GCaMP6f; triangle symbols). **c,** Mean fluorescence image of simultaneously imaged SO layer (with astrocytes) and SP layer (with neurons). **d,** Example behavioral camera image. Blue: Paw movement extracted from subsequent video frames. Red: Mouth movement extracted from subsequent video frames, licking extracted by tongue detection. Green: Pupil diameter visible due to laser light passing from the brain through the eye. **e,** Example of simultaneous recordings, from top to bottom: Subset of neuronal ΔF/F traces (blue, 13 from a total of 107 neurons) extracted from FOV in (c), together with deconvolved spike rates (black) and mean spike rate across all 107 neurons (bottom). Extracted astrocytic ΔF/F traces (6 out of a total of 34 active astrocytic ROIs), together with the mean astrocytic trace across the FOV in (c). Blue: Tracking of the position along the treadmill, together with time points of water rewards; run speed is determined from a rotary encoder, paw movement is extracted from video analysis (blue panel in (d)). Red: Mouth movement and licking are extracted from video analysis (red panels in (d)). Green: Pupil diameter, relative change with respect to median, extracted from video analysis (green panel in (d)).

regression (Fig. 3b; window extent -17...+17 s; see Methods for details). Interestingly, with this analysis the time courses predicted by paw movement or neuronal spike rate were now highly correlated with global astrocytic activity, to a level where they explained global astrocytic activity almost equally well as pupil diameter (Fig. 3d). Notably, mean neuronal spike rate was a much better predictor than the average ΔF/F trace before deconvolution, due to the denoising property of deconvolution[26]. Paw movement was a better predictor than mouth movement, and when licking only (Fig. 2g, right red panel) was used as predictor, predictions degraded even more, consistent with direct observations from behavioral monitoring that mouth-only movements did not reliably evoke astrocytic responses (Movie 4). Analysis of additional experiments that used single-plane imaging to record from astrocytes (SO layer) without neuronal recordings confirmed these results (Fig. S2). Based on these findings, we focus in the following on pupil diameter, paw movement, and mean neuronal spike rate as the best predictors of global astrocytic activity. Overall, predictions were not significantly improved when using multiple regressors for dilated regression (Fig. S3), suggesting mostly redundant regressors. In agreement with the idea of redundant processes, predictions of global astrocytic activity based on the different regressors were highly correlated (Fig. 3e). For example, predictions based on paw movement

bioRxiv preprint doi: https://doi.org/10.1101/2022.08.16.504030; this version posted August 17, 2022. The copyright holder for this preprint (which was not certified by peer review) is the author/funder, who has granted bioRxiv a license to display the preprint in perpetuity. It is made available under aCC-BY-NC 4.0 International license.

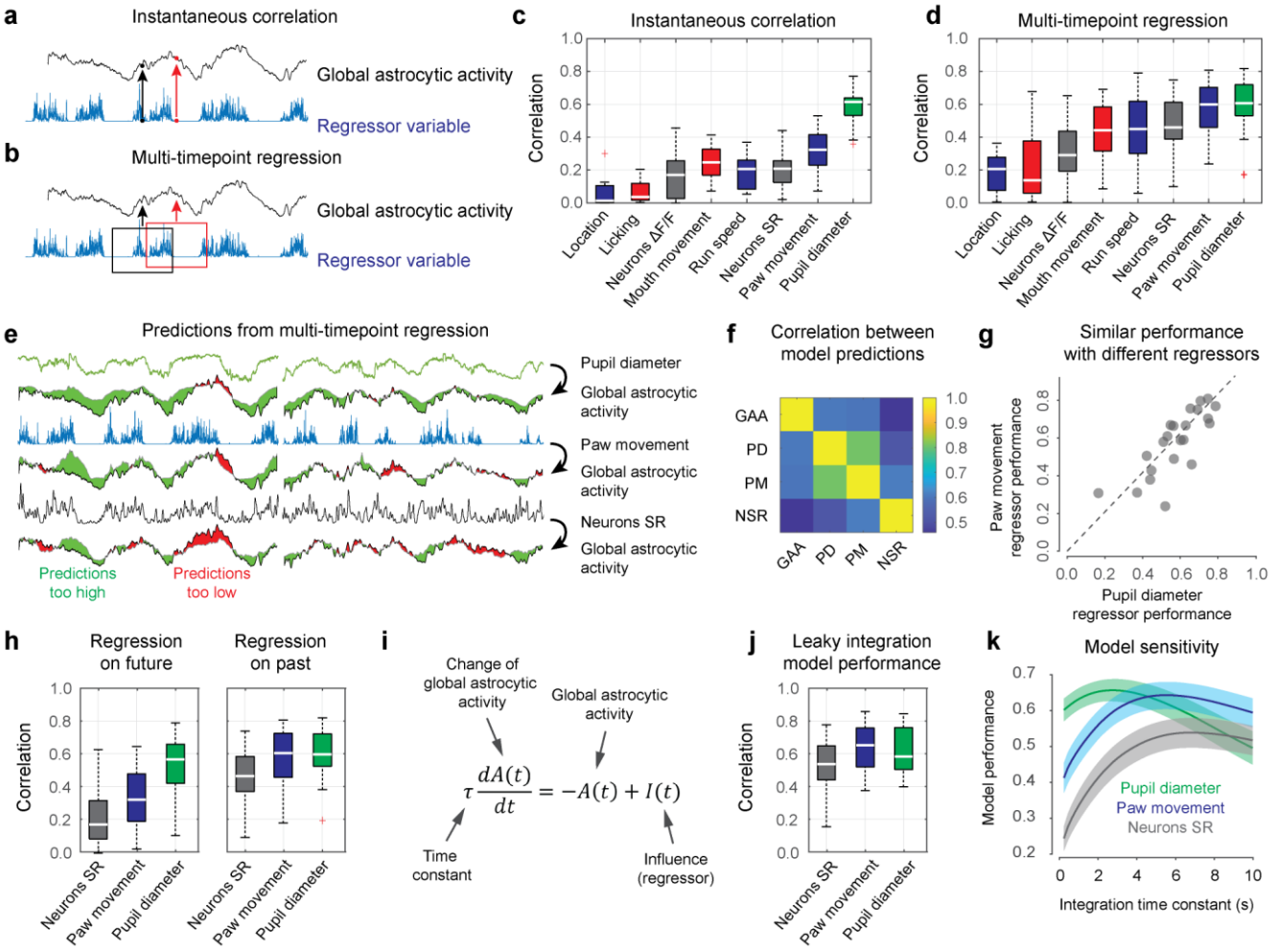

Figure 3. Global astrocytic activity can be well explained by past behavior, mean neuronal spike rate or pupil diameter. **a,** Schematic illustration of instantaneous correlation. A single time point is used to predict a simultaneous astrocytic time point. **b,** Schematic illustration of multi-timepoint regression. A range of data points in a window is used to predict a single time point of astrocytic activity. **c-d,** Performance of various regressors when using instantaneous correlation (c) or multi-timepoint analysis (d) to predict astrocytic activity (n = 22 imaging sessions from 4 animals). The mean neuronal spike rate is abbreviated as 'Neurons SR'. Box plot properties are defined as described in Methods. **e,** Example cross-validated predictions from the three best regressors (pupil diameter, paw movement, mean neuronal spike rate). Green areas indicate when predicted activity is too high, red areas when it is too low. **f,** Average correlation between global astrocytic activity and the activity predicted by the three regressors (GAA, global astrocytic activity; PD, pupil diameter; PM, paw movement; NSR, neurons spike rate). **g,** Example of performance for two different regressors (pupil diameter, paw movement) across sessions (correlation r = 0.79). See also Fig. S4. **h,** Multi-timepoint regression, but using only either future or past time points. **i,** Leaky integration differential equation to model global astrocytic activity A(t) as a function of regressor input I(t), dependent on the integration time constant τ. **j,** Model performance using the leaky integration differential equation. **k,** Model sensitivity with respect to the integration time constant τ (mean ± bootstrapped 90% confidence interval of the mean, determined from 22 imaging sessions).

and pupil were even more highly correlated among each other than with the global astrocytic activity itself (Fig. 3f, 0.76 ± 0.14 vs. 0.59 ± 0.15, mean ± s.d.; p = 0.00026, Wilcoxon signed-rank test). In addition, two regressors typically performed similarly for the same recording session but co-varied across sessions (Fig. 3g; Fig. S4). Together, these analyses highlight that seemingly unrelated behavioral and neuronal variables can explain global astrocytic activity equally well when

bioRxiv preprint doi: https://doi.org/10.1101/2022.08.16.504030; this version posted August 17, 2022. The copyright holder for this preprint (which was not certified by peer review) is the author/funder, who has granted bioRxiv a license to display the preprint in perpetuity. It is made available under aCC-BY-NC 4.0 International license.

non-instantaneous dependencies are considered.

Global astrocytic activity can be explained as a leaky integration of past events

Next, to better understand why multi-timepoint models performed much better than models based on instantaneous correlation, we systematically studied the relative relationship of the observables in time. First, we repeated the regression analysis but used only past or future regressor time points to predict global astrocytic activity. These analyses showed that past but not future time points of paw movement or neuronal spike rate could be used to predict astrocytic calcium transients (Fig. 3h). For pupil diameter, we found a less striking difference between predictors based on past vs. future time points (Fig. 3h) and the multi-timepoint model based on pupil diameter did not exhibit a significant performance increase with respect to instantaneous correlation (cf. Fig. 3c,d; $p = 0.28$, Wilcoxon signed-rank test across 22 sessions from 4 mice). To directly describe the temporal relationship, we attempted to model global astrocytic activity as a temporal integration of mean neuronal spike rate, paw movement, or pupil diameter changes. Instead of using a more complex linear regression with multiple weights for past and future time points as before, we fitted a linear differential equation that simulates global astrocytic activity as a leaky integration of a single variable, with a single free parameter, the time constant τ (Fig. 3i). Interestingly, this simple model explained an even higher amount of variance than the cross-validated regression for the paw movement and neuronal activity regressors (Fig. 3j vs. Fig. 3d; $p < 0.005$ for neuronal spike rate and paw movement, $p = 0.19$ for pupil; Wilcoxon signed-rank test). The integration time constants that were obtained as fit parameters were relatively short for pupil diameter (τ = 2.8 ± 0.5 s; mean ± 90% bootstrapped confidence intervals across sessions) but substantially longer for paw movement (5.6 ± 0.5 s) and neuronal spike rate (6.8 ± 0.5 s). To determine the parameter-sensitivity of the model, we evaluated each model's performance for a range of time constants. This analysis confirmed the longer time constants for paw movement and neuronal spike rate regressors, and, in addition, highlighted a relatively flat peak of the parameter dependency (Fig. 3k). We conclude that global astrocytic activity can be well described as an instantaneous readout of pupil diameter but, alternatively, also as a leaky integration of past neuronal population spike rate or body movement.

Prominent global astrocytic activity is absent during anesthesia

While our analyses do not reveal the processes that causally trigger astrocytic activity, they show that both mean neuronal spike rate, paw movement, and pupil diameter are almost equally reliable readouts of this process and are therefore largely redundant as explanatory variables for global astrocytic activity. Closer examination of the dataset together with additional experiments enabled us to refine our description. First, mean neuronal spike rate was the worst of the three main regressors to explain global astrocytic activity (Fig. 3d,j). In anesthetized animals, consistent with recent results in CA1[30], neuronal spike rates were significantly but only slightly reduced (Fig. 4a,c; 0.14 ± 0.03 Hz vs. 0.09 ± 0.01 Hz; $p = 0.004$, Mann-Whitney ranksum test). At the same time, astrocytic activity was strongly reduced. The global astrocytic activation mode was absent whereas some astrocytes still exhibited local events (Fig. 4b; Fig. S5). Moreover, the mean neuronal spike rate failed to explain global astrocytic activity beyond chance level during anesthesia (Fig. 4d; $p = 0.88$, Wilcoxon signed-rank test), consistent with previous findings that

bioRxiv preprint doi: https://doi.org/10.1101/2022.08.16.504030; this version posted August 17, 2022. The copyright holder for this preprint (which was not certified by peer review) is the author/funder, who has granted bioRxiv a license to display the preprint in perpetuity. It is made available under aCC-BY-NC 4.0 International license.

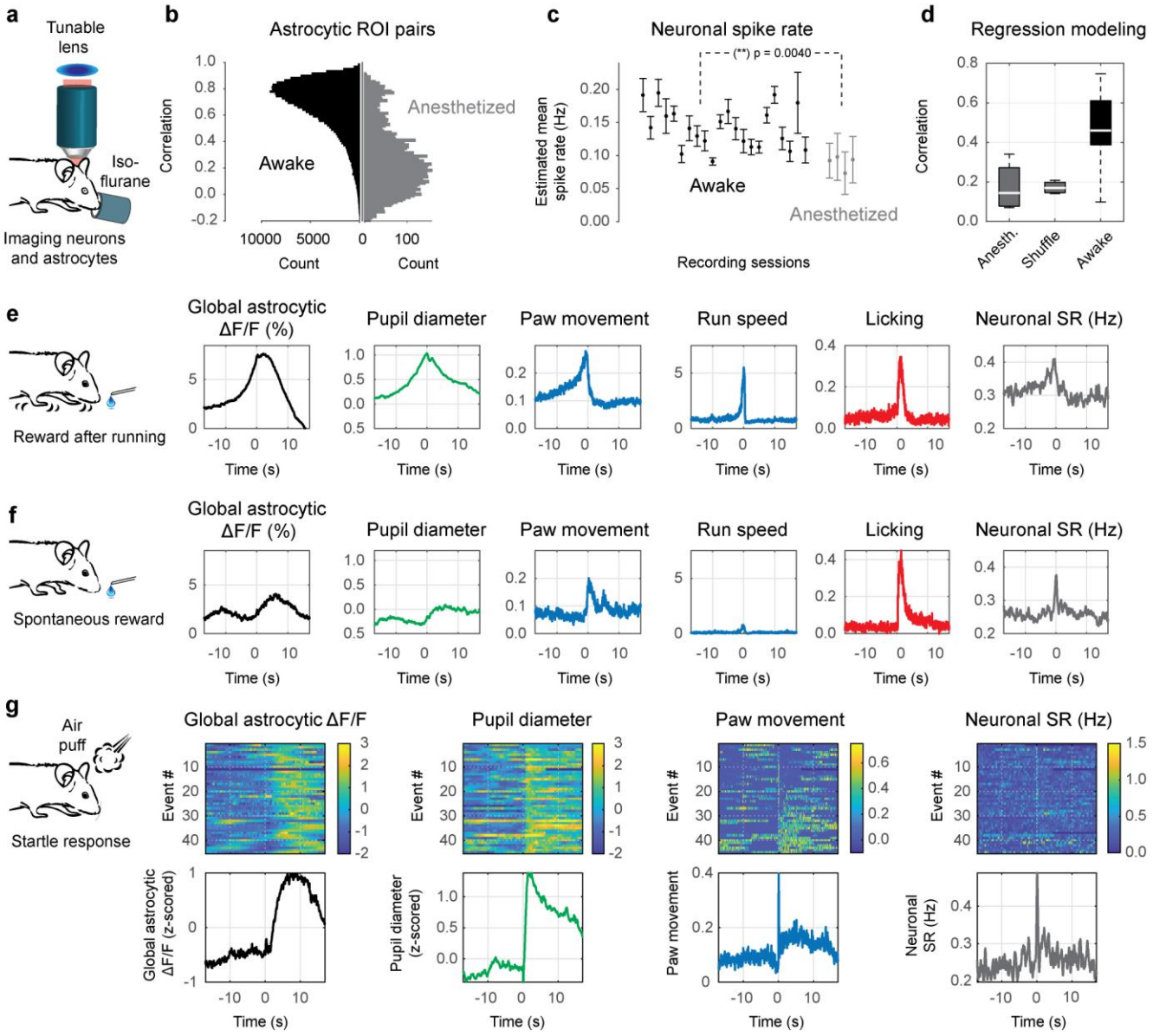

Figure 4. Pupil diameter but not neuronal activity or body movement are reliably coupled to global astrocytic events. a, Simultaneous imaging of astrocytes and neurons during isoflurane-induced anesthesia (1.5% in O_2). **b,** Pairwise correlation between astrocytic ROIs during awake and anesthetized conditions. The awake distribution corresponds to Fig. 1i. **c,** Estimated neuronal spike rate for each awake and anesthetized session (mean ± s.d. across neurons). Comparisons of session means across conditions: p = 0.0040, Wilcoxon ranksum test). **d,** Multi-timepoint regression modeling of global astrocytic activity using neuronal activity as regressor during anesthetized and awake sessions. **e,** Event-triggered average traces for rewards that are obtained at a reward location after running, aligned to reward consumption (average across n = 260 events). All variables with arbitrary scaling (a.u.) unless otherwise indicated. **f,** Event-triggered average traces for spontaneous rewards, aligned to reward consumption. (n = 168). All variables with arbitrary scaling (a.u.) unless otherwise indicated. **g,** Event-triggered traces for air-puff induced startle responses (top: heatmap of individual traces for 45 events; bottom: average across events). Single traces for ΔF/F and pupil diameter are z-scored. Traces in heatmaps are sorted by increasing paw movement during the first 3 s after the air puff.

reported strongly reduced astrocytic calcium levels in cortex during anesthesia[31,11] or during sleep[32]. Global astrocytic activity re-occurred, however, when the animal woke up and started to move

bioRxiv preprint doi: https://doi.org/10.1101/2022.08.16.504030; this version posted August 17, 2022. The copyright holder for this preprint (which was not certified by peer review) is the author/funder, who has granted bioRxiv a license to display the preprint in perpetuity. It is made available under aCC-BY-NC 4.0 International license.

(Fig. S5). These results suggest that it is unlikely that neuronal activity alone is sufficient for the generation of large and coordinated astrocytic activity.

Global astrocytic activity can be better explained by body movement than by navigation

Because of the central role of the hippocampus for navigation, and given the results shown in Fig. 3, it seemed plausible that hippocampal astrocytes are activated mainly during phases of self-generated locomotion associated with expectation of reward, as proposed recently[6]. We inspected a set of externally generated and spontaneous behavioral events to investigate this hypothesis. We found that global astrocytic activity indeed ramped towards the location of an expected reward (Fig. 4e). However, this ramping occurred simultaneously with body movements, locomotion, neuronal activity, and pupil diameter changes (Fig. 4e). A similar, albeit smaller, increase of global astrocytic activity could be seen upon spontaneous rewards that were delivered at random time points (Fig. 4f). Given our regression analysis results (Fig. 3d; in particular, that spatial location is not a good predictor of global astrocytic activity), the more parsimonious explanation of astrocytic activity therefore seems an integration of past events (*e.g.,* movement or internal arousal), rather than an encoding of future reward. In addition, we found that global astrocytic activity was better described by regressing paw movement than by regressing simple locomotion-associated run speed (Fig. 3c), suggesting that past paw movements rather than navigation are "encoded" in global astrocytic activity. In line with that, we found that a purely non-navigational behavior, when the mouse occasionally used its hands to reach for the lick spout, most likely in order to retrieve sugar water residues, consistently elicited an increase of global astrocytic activation despite lack of locomotion (Fig. S6; Movie 5). On the other hand, we also observed that behavioral events without significant body movement resulted in astrocytic activation: In a subset of sessions, we applied a salient, rare and unpredictable stimulus (air puff to the left face) when the animal was sitting still. In some cases, this resulted in movement and running of the animal, together with increased pupil diameter and global astrocytic activation (Fig. 4g), consistent with previous cortical calcium imaging experiments of astrocytes during startle responses[16,17,33,34]. However, in a subset of stimulus applications, the mouse remained immobile or frozen despite the stimulus, while the pupil diameter increased together with astrocytic activity (Fig. 4g, top rows of the sorted traces).

Together, although all three aspects (mean neuronal spike rate, paw movement, and pupil diameter) can be used as predictors, global astrocytic activity can occur in the absence of movement and is not a necessary consequence of neuronal activity (Fig. 4). Our observations support the existing evidence from other brain areas that increased global astrocytic activity is mediated via noradrenergic neuromodulation[13], reflected by an increase of the pupil diameter. This relatively clear picture is complicated by observations of small pupil dilations observed during mouth movements that are not accompanied by global astrocytic calcium signals (Movie 4), which could reflect either the non-linearity of the calcium indicator or a lack of coupling of pupil diameter and astrocytic activity during such subtle behavioral events. Irrespective of these details, our analyses show that global astrocytic activity is not only coupled with pupil diameter as a proxy for neuromodulatory tone, but also with mean neuronal spike rate and self-generated movements, resulting in a meaningful

bioRxiv preprint doi: https://doi.org/10.1101/2022.08.16.504030; this version posted August 17, 2022. The copyright holder for this preprint (which was not certified by peer review) is the author/funder, who has granted bioRxiv a license to display the preprint in perpetuity. It is made available under aCC-BY-NC 4.0 International license.

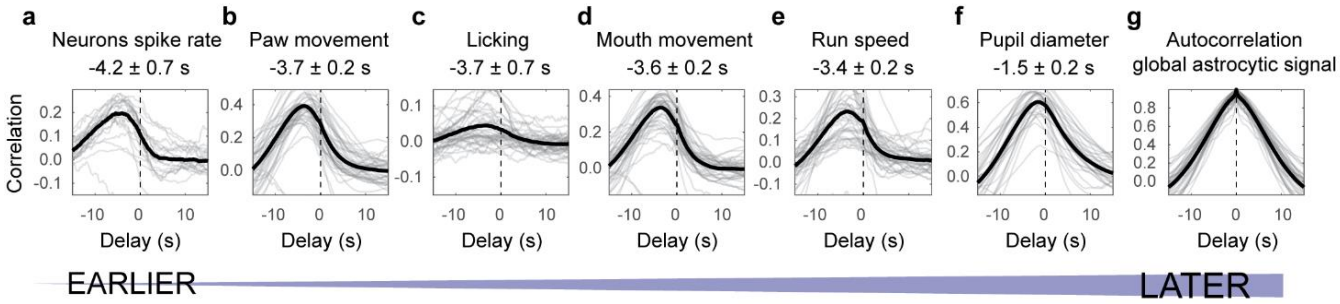

Figure 5. Temporal sequence of neuronal spike rate, motor behaviors, pupil diameter, and global astrocytic activity. Correlation functions were computed between the global astrocytic signal and the variable of interest: neuronal activity (**a**), paw movement (**b**), licking (**c**), mouth movement (**d**), run speed (**e**), pupil diameter (**f**) and astrocytic signal (**g**, autocorrelation). A peak of the correlation function with negative lag indicates that the inspected variable peaked on average earlier than global astrocytic activity. Grey traces are correlation functions extracted from single sessions, black traces are averages across sessions. The delays indicated are median values ± standard error across sessions (n = 22 sessions across 6 animals, except for pupil with 33 sessions across 6 animals and neuronal spike rate with 22 sessions across 4 animals).

functional association, despite a possible absence of causality.

Temporal sequence of events preceding global astrocytic activity

We next aimed to describe the temporal relationship of the observables functionally associated with astrocytic activity more quantitatively. To assess temporal relationships directly from the experimental data without imposing a model, we computed the correlation functions between observables, which enabled us to estimate the delay of any recorded observable with respect to global astrocytic calcium signals (Fig. 5a-g). Strikingly, we found consistent delays as quantified by the peak of the correlation function. Whereas the deconvolved neuronal spike rate peaked first (4.2 ± 0.7 s prior to astrocytic calcium signal; Fig. 5a), paw movements followed with a small delay (3.7 ± 0.2 s prior; Fig. 5b; see also Fig. S7), followed by pupil diameter (1.5 ± 0.2 s prior; Fig. 5f). Together, we found, on average, a consistent and stable sequence of events, from neuronal spike rate changes and various body movements, to pupil diameter changes, to astrocytic activation.

Propagation of astrocytic activity from distal to somatic compartments

Correlation functions average across time points and therefore can reveal temporal relationships that are obscured by variability and noisy single events. To better understand astrocytic activity in single cells, we applied our analysis based on correlation functions not only to the global astrocytic signal but also to the activity of single astrocytic ROIs (which can be either astrocytic somata or active gliapil regions) by computing the correlation function of each astrocytic ROI with the global astrocytic activation. Surprisingly, we observed that the delay of a given astrocytic ROI with respect to the global mode was variable across ROIs but consistent for a given ROI, and could be relatively long (a few seconds) (Fig. 6a,b). To understand the spatial organization of such delays, we projected the measured delays of ROIs onto the spatial map determined by the mean fluorescence image. We found that ROIs with positive delays (activation after the global mode) tended to map onto regions comprising astrocytic somata, while ROIs with negative delays (activation prior to the global mode) mapped onto

bioRxiv preprint doi: https://doi.org/10.1101/2022.08.16.504030; this version posted August 17, 2022. The copyright holder for this preprint (which was not certified by peer review) is the author/funder, who has granted bioRxiv a license to display the preprint in perpetuity. It is made available under aCC-BY-NC 4.0 International license.

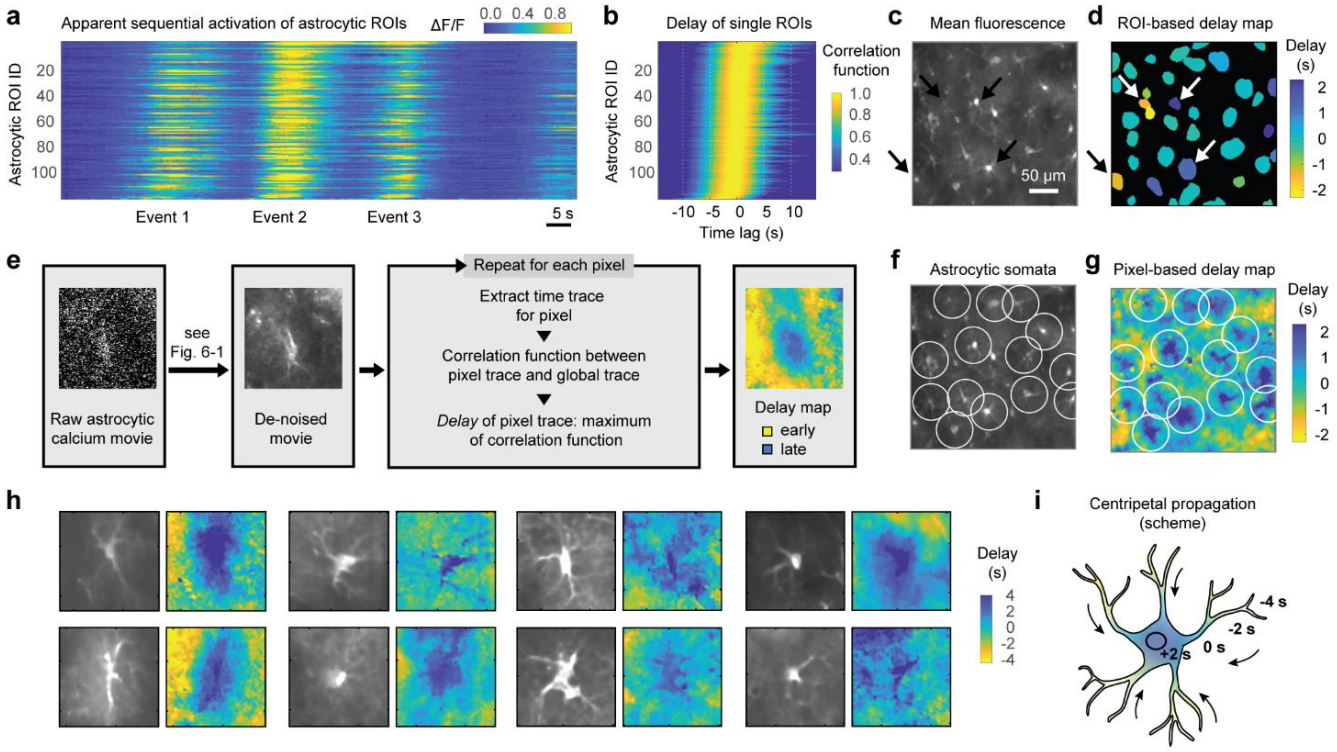

Figure 6. Propagation of astrocytic activity from distal to somatic compartments. a, Excerpt of calcium recording across a population of hippocampal CA1 astrocytes during behavior. Astrocytic ROIs are sorted by the delay of the correlation function with respect to the global mean. An apparent sequential activation of astrocytic ROIs is visible for each of the three events. **b,** Correlation functions of the single astrocytic ROIs, same sorting as in (a). The time window in (a) is only a small part of the activity pattern used to compute the correlation functions. **c,** Excerpt from the mean fluorescence of the astrocytic FOV recording from (a,b). **d,** Delays extracted as maxima in (B), mapped onto the astrocytic ROIs. Right-ward pointing arrows highlight ROIs with strong negative delay (undefined anatomical structure), left-ward pointing arrows highlight example ROIs with strong positive delay (cell bodies). **e.** Processing pipeline for pixel-wise delay maps, consisting of de-noising, pixel-wise computation of the correlation function, extraction of the delay and spatial mapping of each pixel's delay (see Fig. S8). **f,** Same map as in (c), with white circles highlighting anatomically defined astrocytic cell bodies. **g,** Pixel-based delay map corresponding to the anatomy overview in (f). Somatic regions (center of white circles) are activated with a positive delay (blue), gliapil with a negative delay (yellow) with respect to the global astrocytic activity. **h,** Zoom-in to selected delay maps around anatomically identified cell bodies of astrocytes. The side length of each FOV excerpt is approximately 55 µm. See Fig. S9 for more examples and Fig. S10 for entire delay maps. **i,** Schematic illustration of centripetal propagation of astrocytic activity from distal processes to the somatic region.

regions that did not exhibit any clearly distinct structure (Fig. 6c,d).

Next, to analyze the spatio-temporal astrocytic patterns without the bias induced by manually selected ROIs, we attempted to use the time trace of each pixel in the calcium movie to determine a fine-grained delay map on a single-pixel level. To enable such a precise spatio-temporal analysis that is normally prevented by shot noise, we trained and used self-supervised deep networks[35]. This de-noising algorithm takes advantage of the temporally and spatially adjacent pixel values to make an improved estimate of the intensity value of the pixel of interest. This method enabled us to de-noise the raw data and generate meaningful time courses for each single pixel (Fig. 6e; Fig. S8; Movie 6; see Methods for details). The correlation functions of these single-pixel traces with the

bioRxiv preprint doi: https://doi.org/10.1101/2022.08.16.504030; this version posted August 17, 2022. The copyright holder for this preprint (which was not certified by peer review) is the author/funder, who has granted bioRxiv a license to display the preprint in perpetuity. It is made available under aCC-BY-NC 4.0 International license.

global astrocytic signal revealed a smooth map of delays across the FOVs (Fig. 6g; Fig. S10), with features that were obscured in the ROI-based delay map (Fig. 6d). As a striking and surprising feature of these pixel-wise delay maps, delays tended to be negative for gliapil regions devoid of somata and large astrocytic processes, whereas they increased and became positive when approaching the astrocytic somata (Fig. 6f-i; Figs. S9 and S10). This feature of the delay maps indicates that astrocytic activity, on average, propagates from distal, fine processes to the soma, on a timescale of several seconds. Beyond this first-order effect, we also found that a few astrocytic somata did not exhibit such a positive delay, suggesting some heterogeneity of the effect (green arrow heads in Fig. S10a,g). Furthermore, we anecdotally observed that prominent end feet surrounding blood vessels were often activated later than both astrocytic somata and gliapil (white arrows in Fig. S10g,i). Finally, visual inspection of raw movies clearly showed substantial local ongoing activity that cannot be described as a propagation from distal to somatic compartments (*e.g.,* Movies 1, 2 and 6). Therefore, the propagation of activity from distal processes to the central soma dominated the average delay maps but other processes that were averaged out over time also occurred.

Centripetal propagation is conditional on the animal's arousal state

To better understand the function and behavior of this centripetal integration in astrocytes towards the soma, we used the delay maps to extract the average time course of all FOV pixels within a specific range of delays (binned in 1-s bins; Fig. 7a,b). Following the results in Fig. 6, the time course of FOV pixels with negative delays thus reflected activity of distal processes, while the time course of FOV pixels with positive delays reflected activity of somatic regions. Importantly, this analysis enabled us to compare the shape of the same calcium event in putative distal processes vs. somatic regions. To this end, we semi-automatically detected events (typically 15-30 s long; see Methods) and found that many detected events reliably propagated activity from distal processes towards the somatic centers of astrocytes. However, some events started in distal processes but then decayed and failed to activate the cell body (Fig. 7c), indicating a thresholding of centripetal propagation. To quantify whether a given event propagates to the center of the cell or not, we computed the "slope" of propagation for each event, determined by a linear fit of the activity peak of the ΔF/F trace vs. the respective delay, such that a negative slope indicates a non-propagating, fading event whereas a neutral or positive slope indicates a centripetally propagating event that activates the soma (Fig. 7c, inset). While the majority of events exhibited a slope slightly above or around zero, indicating stable propagation towards the center, some events exhibited a negative slope, reflecting a failure to activate the soma (Fig. 7c-e; Fig. S11). These non-propagating events only occurred when the associated pupil diameter (pupil diameter z-scored within each session) was rather low (Fig. 7d) and, also the astrocytic calcium event itself (Fig. S12a). An increased or decreased pupil diameter could reflect either the relatively long-lasting pupil diameter changes during an alert or quiescent state, or phasic pupil diameter changes upon salient sensory or self-generated events. We isolated the phasic component by computing the rectified derivative of pupil diameter as a 'saliency score'. As for the pupil diameter (Fig. 7d), propagation slopes were negative only for low values of the saliency score (Fig. S12b). Together,

bioRxiv preprint doi: https://doi.org/10.1101/2022.08.16.504030; this version posted August 17, 2022. The copyright holder for this preprint (which was not certified by peer review) is the author/funder, who has granted bioRxiv a license to display the preprint in perpetuity. It is made available under aCC-BY-NC 4.0 International license.

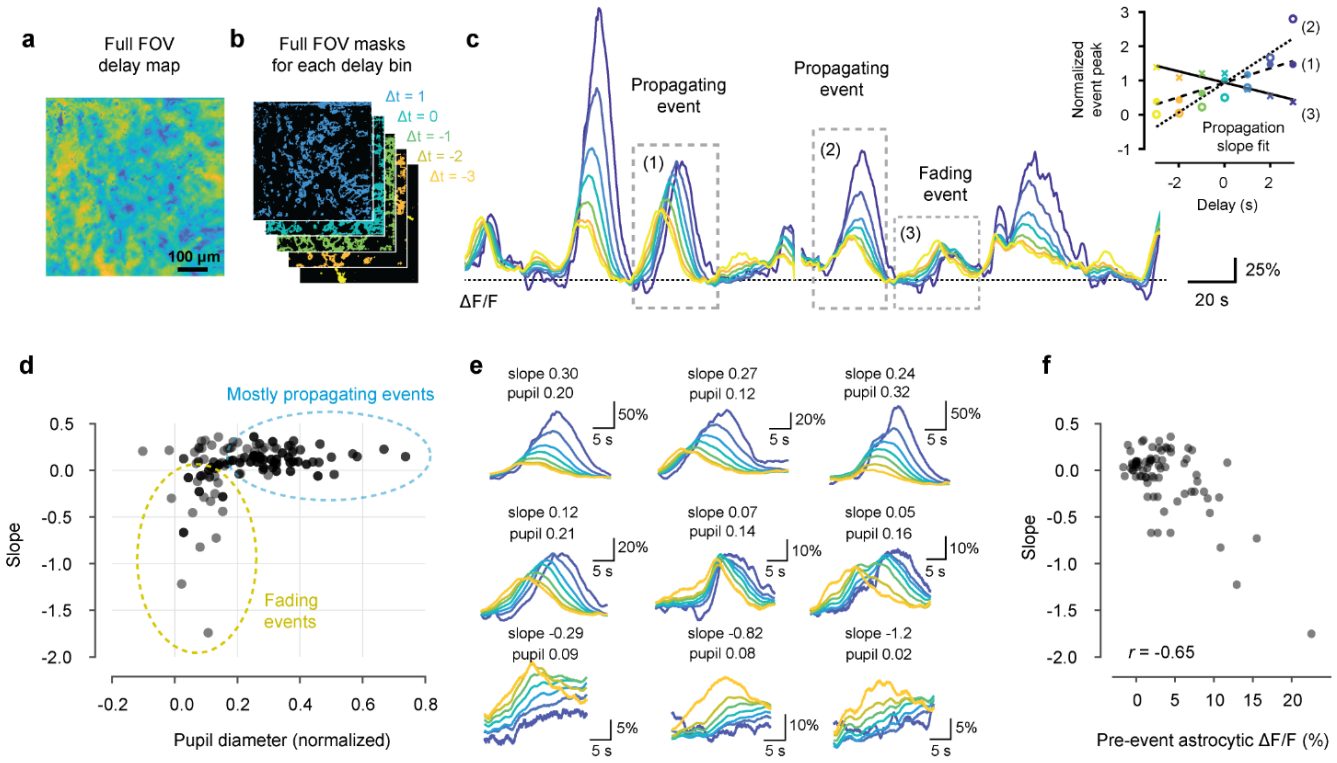

Figure 7. Centripetal propagation of activity in astrocytes is conditional on arousal state and cell-intrinsic calcium signaling history. a-b, A smoothed delay map of the entire FOV is binned according to the delays of each pixel (Δt = 1 corresponds to the 0.5…1.5 s interval). **c,** The delay bin masks (b) are used to extract global astrocytic traces from pixels with a specific delay from the de-noised recording (color-coding). Due to centripetal propagation, yellow traces represent gliapil and blue traces astrocytic somata. Some calcium events propagate to somata (events (1) and (2)), while others do not (event (3)), quantified by a positive or negative propagation slope, respectively (inset). Therefore, centripetally propagating and non-propagating events can be determined by the slope of peak activity with respect to delay. **d,** Propagation slope of events plotted against the normalized pupil diameter as a proxy for arousal state. Each data point corresponds to a single event. **e,** Example events are plotted in the order of sorted slope values. See Fig. S11 for additional example events. **f,** Pre-event astrocytic ΔF/F, averaged across the 20 s prior to the event, is negatively correlated with the slope value. Only data points with normalized pupil diameter < 0.2 from (d) were included for this panel.

these analyses suggest that centripetal integration of astrocytic activity is conditional on the animal's state and facilitated by high levels of noradrenergic tone and arousal.

Centripetal propagation is conditional on cell-intrinsic calcium signaling history

We noticed that some events with similar normalized pupil diameter or saliency score were propagated to the soma (slope > 0), but others not (slope < 0; Fig. 7d, Fig. S12). Previous studies have shown that the strength of astrocytic activation depends on past activity, described as a "refractory period" or cell-intrinsic "memory trace" dependent on intracellular Ca^{2+} store dynamics[20,36,19]. Indeed, we found that the slope of events associated with low arousal (normalized pupil diameter < 0.2; Fig. 7d) was negatively correlated with the mean astrocytic ΔF/F during the 20 s prior to the investigated event (Fig. 7f). Together, these results show that astrocytes integrate activity in a centripetal manner, and that this propagation is conditional not only on the animal's state as measured with

bioRxiv preprint doi: https://doi.org/10.1101/2022.08.16.504030; this version posted August 17, 2022. The copyright holder for this preprint (which was not certified by peer review) is the author/funder, who has granted bioRxiv a license to display the preprint in perpetuity. It is made available under aCC-BY-NC 4.0 International license.

the pupil diameter, but also on the prior history of astrocytic activation.

The strength of centripetal propagation can be variable across astrocytes

Finally, to investigate the variability of centripetal propagation across cells and to better understand possible cell-intrinsic effects, we extended our analysis to single astrocytic domains. To this end, we used seeded watershed segmentation to approximate distinct astrocytic domains (see Methods) and to quantify centripetal dynamics within each of the individual domains (Fig. S13a-d). The majority of astrocytic domains followed a correlated pattern that consisted of an either propagating or non-propagating behavior for a given event across most putative astrocytic domains (Fig. S13e). This correlation among putative domains only weakly depended on the inter-domain distance (Fig. S13f). Interestingly, the propagation slope in some astrocytic domains was much higher than for other domains during the same event (Fig. S13d,g), hinting at a possible continuous distribution of the strength of somatic activation upon centripetal propagation. As another interesting and related observation, we noticed astrocytes that did not follow the global pattern, *e.g.,* exhibiting a centripetally propagating event while most other domains exhibited non-propagative behavior (Fig. S13d,h). These results suggest that conditional centripetal propagation of activity, while mostly synchronized across the population of astrocytes, is a process that has the potential to occur separately in each astrocytic domain and could therefore be determined independently for each astrocyte.

Discussion

In this study, we provide evidence that hippocampal astrocytes can be interpreted as integrators of information about past events on a time scale of seconds. We demonstrate that this slow integration proceeds from distal processes to the soma, and we further show that this centripetal propagation is conditional both on the state of the astrocyte (past calcium transients) and the state of the animal (level of arousal). This conditional centripetal propagation in astrocytes represents a new integration principle and establishes astrocytes as computational units of the brain that act on a time scale that is much slower than for neurons.

The global astrocytic mode dominates in hippocampal CA1 *in vivo*

Recent evidence in cortical and cerebellar brain areas has shown that astrocytic activity *in vivo* is dominated by a global mode of activation most likely mediated by noradrenergic neuromodulation[16,17,8,37,19,38]. Here we show that such a global pattern also describes the astrocytic population across hippocampal CA1 layers in awake but not anesthetized mice (Fig. 1; Fig. 4a-d). Consistent with this finding, noradrenergic axonal terminals in hippocampal CA1 were recently shown to be highly correlated in their activity, suggesting a global neuromodulatory effect[39]. In our experiments, calcium signals emerged quasi-simultaneously across the entire field of view (Fig. 6; Fig. S10), consistent with the idea of a common, global influence converging on astrocytes, and arguing against a dominant role for wave-like propagation of activity within the syncytium of astrocytes through gap junctions (reviewed *e.g.* by ref. [9]). In addition to the global activity, we also observed prominent local events in subsets of astrocytes or individual astrocytes that were independent of

bioRxiv preprint doi: https://doi.org/10.1101/2022.08.16.504030; this version posted August 17, 2022. The copyright holder for this preprint (which was not certified by peer review) is the author/funder, who has granted bioRxiv a license to display the preprint in perpetuity. It is made available under aCC-BY-NC 4.0 International license.

global events (Fig. 1f,g; Fig. S5) and rich ongoing local activity in distal processes that could only be partially resolved using two-photon imaging (Movies 1, 2 and 6), consistent with converging evidence that astrocytic calcium events *in vivo* are prominent in distal processes[9–11,40,41].

Astrocytic activity reflects neuromodulation, neuronal activity, and movement

Astrocytic calcium signals in rodents have been shown to exhibit remarkable features that seem to be partially conserved across brain regions. First, astrocytes become globally active as a consequence of salient stimuli, most likely mediated by noradrenergic neuromodulation. While there is to our knowledge no direct evidence that neuromodulation influences specific behaviors in mammals via astrocytic activation, such evidence has been found in zebrafish larvae and drosophila[42,43]. Second, astrocytes in neocortex and cerebellum are activated upon movement or locomotion of the animal[18,20,17,19]. Connecting the aspects of arousal and movement, the temporal relationship of body movements and locomotion have been shown to be closely related to pupil diameter changes[15,44,45]. Pupil diameter, notably, is considered a proxy of noradrenergic (and also cholinergic) modulation, and was found to be delayed by approximately 1 s with respect to the activation of noradrenergic axon terminals[27]. Third, a causal effect of neuronal activity on astrocytic activity has been proposed, albeit with mixed evidence in favor or against[7,40,37,8], including the interesting idea that the combined effect of neuronal and noradrenergic activity can result in astrocytic activation[17,46]. Here, we have studied these three processes systematically and simultaneously, together with the activity of hippocampal astrocytes (Fig. 2). We find that all these factors – local neuronal activity, body movement, and pupil diameter as a proxy for neuromodulation – can explain a high degree of variability of the astrocytic signal. However, this is only true if non-instantaneous metrics are employed, taking into account the influence of past events on the present astrocytic signal (Fig. 3). The strong redundancy of these three explanatory variables might be surprising but is possibly related to a common origin of movements, movement-related neuronal activity, and neuromodulatory signals in brain stem circuits[47].

A closer examination of different behavioral states and events (Fig. 4) showed that the observed global astrocytic activation can occur without movement and can be completely absent during anesthesia, where neuromodulatory tone is low while substantial neuronal activity is present. These observations support the idea of a central role of neuromodulation rather than neuronal activity or movement to gate the emergence of global events.

Hence, our systematic investigation reveals candidates for coupling of behavioral and neuronal variables to astrocytic activation that might not be causal, *i.e.*, sufficient for activation, but still physiologically relevant for astrocyte function. Our quantitative description of the temporal sequence of the observed variables and events (Figs. 4,5) provides a scaffold to understand and further probe such functional coupling.

A caveat for studying the role of astrocytes in behaving animals

Our systematic description may also serve as a caveat for future functional studies of astrocytic activity *in vivo*. Systems neuroscience has only recently become more broadly aware that neuronal signals across the entire brain might be

bioRxiv preprint doi: https://doi.org/10.1101/2022.08.16.504030; this version posted August 17, 2022. The copyright holder for this preprint (which was not certified by peer review) is the author/funder, who has granted bioRxiv a license to display the preprint in perpetuity. It is made available under aCC-BY-NC 4.0 International license.

explained by global or specific motor signals[14,15]. As a reflection of this insight, typical systems neuroscience studies now regularly consider task-irrelevant movement[48], internal states[47] or mouse-specific strategies[49,50] as confounding variables or as features of neuronal representations. We hope that our systematic study, together with other recent astrocyte-focused studies[19], will raise this awareness also for the field of astrocyte systems neuroscience, and will establish that the disentanglement of these processes, which has turned out to be challenging for neurons[47], is not easier for astrocytes. For example, we show that paw movement is a better predictor of astrocytic activity compared to simple locomotion or running speed; therefore, video monitoring of behaviors should be considered more reliable for the observation of confounding motor movements than the measurement of pure displacement (Fig. 3c, Fig. S2). In addition, we find that instantaneous measures of coupling fail to capture the delayed relationships of astrocytic signals with movement and neuronal activity (Fig. 3c).

As another caveat from a more technical perspective, we find it important to point out that imaging conditions and labeling strategies might have strong and undesired effects on results obtained with astrocytic calcium imaging. For example, astrocytic somata that are slightly out of focus may be more strongly contaminated by the surrounding gliapil, resulting in temporally shifted calcium transients (Fig. 6). Similar concerns apply to imaging conditions where resolution is degraded due to imaging depth or imaging modality and therefore results in mixed somatic and gliapil signals.

In the light of these findings and analyses, previous studies claiming specific computational roles of hippocampal astrocytes, *e.g.*, for reward or place encoding[5,6], might have to be reconsidered and will require careful controls to validate their findings.

Unbiased analysis using global astrocytic activity as a reference

The complex and often seemingly independent activity patterns in the fine processes of individual astrocytes make it challenging to use ROI-based methods for the analysis of astrocytic calcium signals. Recent years have seen a surge of excellent tools specifically designed for the analysis of astrocytic calcium imaging. However, these tools are based either on discrete spatial ROIs[34,51] or on discrete events[52,53], in both cases requiring definition of an event via an arbitrary criterion. Here, we use a method to compute pixel-wise delay maps with respect to a global reference (the global astrocytic activity). Our delay map analysis takes advantage of self-consistent denoising methods [35], uses the averaging power of correlation functions and projects the extracted properties of the correlation function onto the anatomical map, pixel by pixel (Fig. 6). Moreover, the resulting map can be used for the extraction of fluorescence traces based on the extracted properties assigned to each pixel (Fig. 7). This workflow was the enabling factor for our analysis of centripetal propagation, and in general can be used for the unbiased extraction of average spatio-temporal activity patterns. This method therefore provides an approach that is complementary to discrete ROI- or event-based analysis.

Conditional centripetal integration in astrocytes

The most striking feature of astrocytes is their star-shaped morphology. Here we provide

bioRxiv preprint doi: https://doi.org/10.1101/2022.08.16.504030; this version posted August 17, 2022. The copyright holder for this preprint (which was not certified by peer review) is the author/funder, who has granted bioRxiv a license to display the preprint in perpetuity. It is made available under aCC-BY-NC 4.0 International license.

evidence that the soma as the center of this star-shape might act as an integration hub of salient information. First, we show that astrocytic activation can be well described by a simple leaky integration differential equation with the integration time constant as a single parameter (Fig. 3k-j). We systematically measure the delay of astrocytic activity with respect to other observed variables and show that neuronal activity, movement, and pupil changes precede astrocytic activity in a sequence with consistent delays (Fig. 5), in line with previous findings that showed delayed activation of astrocytic somata with respect to external stimuli or self-generated movement[20,19,8,46,16,17]. Second, we show that the global astrocytic activity, which reflects this integration, can be described not only as a temporal but also as a spatial pattern that consists of activity propagating from distal astrocytic processes to the respective soma on a timescale of several seconds (Fig. 6). Consistent with the idea of earlier distal activations, a few recent studies have found that low-latency activation of astrocytes can occur in fine distal processes[11,10,54]. Interestingly, it has been shown in hippocampal slices that calcium events are often restricted to fine processes but expand for stronger stimuli[55], and sometimes invade the somatic region[11]. It has been hypothesized that larger events result from the integration of smaller local calcium signals and that such integration is thresholded by the stimulus intensity[56]. In our experiments, we systematically collected evidence in behaving animals that calcium events in distal astrocytic processes can either propagate or not propagate to the more proximal and somatic compartments. Our analyses indicate that this propagation is conditional on at least two factors: it is facilitated for higher levels of arousal induced by recent salient self-generated or externally driven events; in addition, it is impeded for already elevated calcium concentrations in the respective astrocyte (Fig. 7). Together with previous evidence that calcium concentration changes in late- but not fast-responding astrocytic regions *in vivo* depend on both IP_3 [10,34] and noradrenergic signaling[10], our observations put forward the hypothesis that calcium signals in astrocytic processes are driven predominantly by local synaptic activity and then propagate to the soma in an IP_3-dependent manner only when saliency is communicated through noradrenergic signals. Together, these results suggest a new principle of slow and conditional spatio-temporal integration of past salient events in hippocampal astrocytes. More generally, these findings show that astrocytes can operate as computational units that integrate information from their processes in a conditional manner.

A role for astrocytes to slowly process past events

Neurons not only integrate information from their processes in the soma but also convey the output of this process, the action potential, via their axon to connected neurons. Our finding of central integration of information in astrocytes therefore raises the question about the output generated upon centripetal activation of the astrocytic soma. Close inspection of the properties of centripetal integration might help to role of such an output. As a first property, global astrocytic activity can be described as an integration of past salient events, *e.g.*, a startle response or self-generated movement. Second, the centripetal propagation of astrocytic activity is closely associated with pupil dilation and therefore is likely to depend on neuromodulation and arousal. Third, centripetal propagation acts on a time scale of seconds rather than milliseconds, arguing against a specific role in low-latency neuronal

bioRxiv preprint doi: https://doi.org/10.1101/2022.08.16.504030; this version posted August 17, 2022. The copyright holder for this preprint (which was not certified by peer review) is the author/funder, who has granted bioRxiv a license to display the preprint in perpetuity. It is made available under aCC-BY-NC 4.0 International license.

computations and for a role in processes that act on longer time scales. Modulation of neuronal plasticity is a plausible candidate for such a process, since it acts on behavioral timescales[57] and takes place upon salient events[58]. Such modulation has been studied for hippocampal and other astrocytes both *in vitro*[59–61] and more recently also *in vivo*[62–66]. It remains open what output signals may be triggered by somatic activation of astrocytes, potentially instantiating feedback modulation of the surrounding neuronal processes. A possible astrocytic output signal that could fulfil this role and warrants further investigation in the context of centripetal integration is gliotransmission, the astrocytic release of *e.g.* glutamate[67–70], D-serine[59,60,71] or lactate[72,73], in particular since this process has been found to be prominently involved in neuronal plasticity[56,74]. Centripetal integration of past events in astrocytes therefore seems to be a plausible candidate mechanism to conditionally mediate or modulate neuronal plasticity on a behavioral time scale.

bioRxiv preprint doi: https://doi.org/10.1101/2022.08.16.504030; this version posted August 17, 2022. The copyright holder for this preprint (which was not certified by peer review) is the author/funder, who has granted bioRxiv a license to display the preprint in perpetuity. It is made available under aCC-BY-NC 4.0 International license.

Methods

Animals and surgery

All experimental procedures were carried out in accordance with the guidelines of the Federal Veterinary Office of Switzerland and were approved by the Cantonal Veterinary Office in Zurich. We used adult male and female 4-6 month old Thy1-GCaMP6f (GP5.17, ref. [25]) and wild-type C57BL/6 mice. Mice were provided with analgesia (Metacam 5 mg/kg bodyweight, s.c.) prior to surgery. Anesthesia was induced using isoflurane (5% in O_2 for induction, 1-2% for maintenance during surgery), and the body temperature was maintained at 35-37°C using a heating pad. For surgeries, shaving cream was applied to the dorsal head above the brain, and an incision was made into the skin after local application of lidocaine. To induce expression of GCaMP6s in CA1 hippocampal astrocytes, an injection of AAV virus (ca. 200 nL of ssAAV9/2-hGFAP-hHBbI/E-GCaMP6s-bGHp(A), titer $1.0x10^{13}$ vg/mL; Viral Vector Facility, University of Zurich) was made in hippocampal CA1 (coordinates: AP -2.0 mm, ML -1.5 mm from Bregma, DV -1.3 from the surface of the dura). The injection pipette was left in place after injection for at least 5 min to prevent reflux. A suture was made to close the skin above the skull, and reopened after two weeks to implant the hippocampal window as described previously by others[75] and ourselves[76,77]. Briefly, to expose the brain, a 3-mm diameter ring was drilled into the skull, centered at the previous injection site but avoiding interference with the midline head bone structures. To provide a basis for attachment, two thin layers of light-curing adhesive (iBond Total Etch, Kulzer) were applied to the skull, followed by a ring of dental cement (Charisma, Kulzer) to prevent overgrowth of the preparation with skin. A 3-mm diameter biopsy punch (BP-30F, KAI) was inserted into the exposed brain until it reached the corpus callosum and left in place for at least 5 min to stop bleeding. Damage to deeper structures was avoided by a rubber stop added to the punch. Then, a flatly cut off injection cannula (Sterican 27G, B. Braun) connected to a vacuum pump was used to carefully remove the cortex in the exposed region until the white-red stripes of the corpus callosum became visible. The corpus callosum, different from previous studies targeting deeper regions[76], was left intact. Bleedings, if they occurred, were stopped with absorbant swabs (Sugi, Kettenbach) and hemostatic sponges (Spongostan, Ethicon) before further surgery steps were performed. Then, a cylindrical metal cannula (diameter 3 mm, height 1.2-1.3 mm) attached with dental cement to a 0.17-mm thick coverslip (diameter 3 mm) was carefully inserted into the cavity and fine-positioned with a small-diameter glass capillary attached to the stereotaxic frame. When no further bleeding occurred, the hippocampal window was fixed in place using UV-curable dental cement (Tetric EvoFlow, Ivoclar) that was inserted into the gaps between the skull and the cannula. Finally, tissue glue (Vetbond, 3M) was used to connect the animal's skin with the ring of dental cement (Charisma). A double wing-shaped head bar was attached to the Charisma ring using dental cement (Tetric EvoFlow) directly after the surgery or in a separate surgery session. After surgery, animals were monitored for 3 days with application of antibiotics (2.5% Baytril in drinking water, Vetpharm), and analgesics (Metacam, 5 mg/kg, s.c.) administered when necessary.

Two-photon microscopy

A custom-built two-photon microscope was used to monitor calcium signals in astrocytes and neurons in either a single or multiple layers of CA1, while the animal was spontaneously running on a linear treadmill. A femtosecond-pulsed laser (MaiTai,

bioRxiv preprint doi: https://doi.org/10.1101/2022.08.16.504030; this version posted August 17, 2022. The copyright holder for this preprint (which was not certified by peer review) is the author/funder, who has granted bioRxiv a license to display the preprint in perpetuity. It is made available under aCC-BY-NC 4.0 International license.

Spectra physics; center wavelength tuned to 911 nm; power below the objective 20-40 mW) was sent through a scan engine consisting of a 8-kHz resonant scanner (Cambridge Technology), a 2x magnifying relay lens system, and a slow galvo scanner (6215H, Cambridge Technology), to a dedicated scan lens (S4LFT0089/98, Sill Optics) and a tube lens (Ploessl lens system consisting of two 400-mm focal length achromatic doublet lenses; AC508-400-AB, Thorlabs) before entering the objective's back aperture. Either a 16x (CFI75 LWD 16X W, NA 0.8, WD 3.0 mm; Nikon) or a 40x objective (CFI Apo NIR 40X W, NA 0.8, WD 3.5 mm; Nikon) were used for calcium imaging. The 16x objective provided a larger field of view (600 µm side length) but the back aperture was slightly underfilled, resulting in an axial resolution of 4-5 µm (FWHM). The 40x objective allowed us to overfill the back aperture, resulting in an improved axial resolution of 2-3 µm (FWHM) at the cost of a reduced FOV (200 µm side length). The 40x objective configuration also enabled the use of a small-aperture tunable lens (EL-10-30-C, Optotune) together with an offset lens (f = -100 mm) just before the back focal plane to enable fast z-scanning over a z-range of up to 300 µm as described previously[23]. Imaging was performed in a single plane at a rate of 30.88 Hz (512 x 622 pixels). Volumetric rates were reduced accordingly for dual-plane (15.44 Hz) and triple-plane imaging (10.29 Hz). Scanning and data acquisition was controlled with custom-written software programmed in C++ (http://rkscope.sourceforge.net/, ref. [78]).

Behavioral setup

The treadmill consisted of two custom-designed light-weight wheels, one of which was attached to a rotary encoder (4-mm shaft optical rotary encoder, Phidgets, USA) to measure locomotion of the animal. A 130 cm long and 5 cm wide velvet belt (88015K1, McMaster-Carr) was equipped with sensory landmarks consisting of self-sticking elements, velcro strips and hot glue. A metal tape attached to a single location of the back side of the belt was used as a reflector for an IR sensor to provide a spatial reference signal in order to track the location of the animal on the belt. IR light (LIU850A, Thorlabs) together with a camera (DMK23UP1300, The Imaging Source, recording at 30 Hz; 16-mm EFL objective MVL16M23, Thorlabs) was used to monitor the animal's behavior during the experiment. In a subset of experiment sessions (33 out of 42), a small and partially shielded UV LED (LED370E, Thorlabs) was directed towards the right eye of the animal, resulting in a less dilated pupil and allowing for pupil segmentation from the behavioral video. Rewards in form of sweetened water (30% sugar) were provided through a metal lick spout to the animal at a specific location of the belt that remained unchanged across sessions. Reward delivery was controlled by a solenoid valve (VDW22JA, SMC) that was gated by a relay circuit (Sertronics Relais Module, Digitech). Mice were free to consume the reward whenever they wanted, immediately after reward delivery or later. If mice did not retrieve a reward for 50 s through running, a spontaneous reward was delivered. Reward delivery time points were automatically recorded in the software, and reward consumption (first contact of the mouse's tongue with the water drop) was manually detected for each reward from video monitoring. The time of reward consumption was used for the analyses in Fig. 4e,f. In a subset of experiments, brief air puffs to the left side of the animal's face as additional sensory cues were provided randomly and rarely (maximally once per minute) without predictive cue. To enable the disentanglement of arousal generated by air puffs and movement, air puffs were only applied when the animal was not running for ≥10 s.

The behavioral setup was controlled using custom code written in Python, which controlled valves,

bioRxiv preprint doi: https://doi.org/10.1101/2022.08.16.504030; this version posted August 17, 2022. The copyright holder for this preprint (which was not certified by peer review) is the author/funder, who has granted bioRxiv a license to display the preprint in perpetuity. It is made available under aCC-BY-NC 4.0 International license.

camera triggers, and microscope acquisition start, and recorded the position of the rotary encoder, the IR sensor for absolute position and behavioral events like air puffs or water rewards. The temporal offset and relative recording speed of the camera with respect to two-photon scanning were calibrated in a separate experiment where both the behavioral camera and the two-photon software recorded the same signal of a flashing light.

Behavior training and imaging experiments

One week before experiments, drinking water of mice was supplemented with citric acid (2% of volume) to motivate the mice during the running task[79]. Mice were handled by the experimenter for 15-20 min per day for 3 days without exposure to the behavioral setup. Afterwards, they were accustomed to the behavioral setup and the lick spout. For the next 3-7 workdays, depending on the animal's ability to participate in the task without being stressed, mice were trained to sit or run on the treadmill while being head-fixed. When animals readily ran on the treadmill and consumed sugar water rewards for 15-20 min, imaging experiments were performed.

A behavioral session lasted in total for 15-35 min and consisted of 140 s-long recording segments, spaced by short breaks of 5-20 seconds due to limitations of the two-photon microscope software. The imaging plane was chosen to lay in the central part of *stratum oriens* of CA1 and to clearly contain visible astrocytic somata if possible. For dual-plane imaging of neurons and astrocytes, the first imaging plane was centered at the pyramidal cell layer of CA1, and the second imaging plane 60-90 µm more dorsally. For triple-layer imaging of astrocytes, imaging planes were spaced approximately 70-80 µm from each other, with the central plane residing in the pyramidal cell layer. For triple-plane imaging during anesthesia, two imaging planes spaced by 10-15 µm were positioned in the pyramidal layer of CA1 such that not the same neurons were sampled in both planes and the third plane 60-90 µm more dorsally. Different sessions were performed on different days, and the FOV was changed between days.

Histology

Animals were administered a lethal dose of pentobarbital (Ekonarcon, Streuli) and transcardially perfused with 0.1 M phosphate standard solution (PO4) followed by 4% paraformaldehyde (PFA, in 0.1 PO4). 60-µm thick coronal brain sections were stained with DAPI and anti-GFAP (primary AB rabbit-anti-GFAP 1:1000, secondary AB anti-rabbit with Cy3 1:250) and imaged with a confocal laser-scanning microscope (Olympus FV1000). Three separate channels recorded the nuclear stain DAPI, the intrinsic GCaMP6s of virally induced GFAP-based expression, and the astrocytic antibody staining of astrocytes with Cy3.

Calcium imaging post-processing

Raw calcium imaging movies were spatially resampled to remove the distortion induced by non-linear sinusoidal scanning in the x-axis. Then, rigid movement correction in the xy-plane was applied[80]. Analyses in Fig. 1 were based on manually defined ROIs; analyses in Figs. 3-5 on the global astrocytic activity, which we define as the average ΔF/F signal across the population of astrocytes within the FOV; and analyses in Figs. 6 and 7 were based on pixel-based activity traces (described below). Active ROIs were extracted manually with a previously described toolbox (https://github.com/PTRRupprecht/Drawing-ROIs-without-GUI, ref. [81]), based on anatomical features of the mean fluorescence, as well as on the map of local correlations which highlights correlated spatially close pixels[82]. For neuronal recordings, both active and inactive neuronal somata were

bioRxiv preprint doi: https://doi.org/10.1101/2022.08.16.504030; this version posted August 17, 2022. The copyright holder for this preprint (which was not certified by peer review) is the author/funder, who has granted bioRxiv a license to display the preprint in perpetuity. It is made available under aCC-BY-NC 4.0 International license.

included to provide an approximately unbiased estimate of neuronal spike rates. For dual-layer imaging of both neurons (GCaMP6f) and astrocytes (GCaMP6s), bleedthrough of the gliapil signal in the pyramidal layer resulted in a slow contaminating signal superimposed onto the neuronal signals. We used the mean fluorescence in a 15-pixel wide surround region of the respective neuronal ROI to linearly regress away the astrocytic contamination. Next, deconvolution of the neuronal traces with a deep network trained on a large ground truth dataset (CASCADE; ref. [26]) was performed in Python, suppressing shot noise unrelated to spike-evoked calcium signals as described before[26], but also discarding non-neuronal signal components like residual slow components stemming from astrocytes.

For astrocytic recordings, all clearly visible astrocytic cell bodies were selected as ROIs, but also active gliapil regions that showed a spatially coherent response as seen by the map of local correlations. Processes that were putatively part of a single astrocyte due to correlated activity as seen by the map of local correlations were included in a single ROI. Contamination of the GCaMP6s signals through neuronal signals (GCaMP6f) in dual-layer recordings were mostly negligible. Only in a small subset of experiments, the basal dendrites of pyramidal cells were bright enough to have a visible impact on the astrocytic imaging plane in *stratum oriens*. Due to the known leakiness of the GFAP promotor, also a very sparse set of interneurons was labeled with GCaMP6s. These rare cells were identified based on their distinct morphology in the mean fluorescence image (see Fig. S10b for an example) and based on their quickly fluctuating signals which were clearly distinct from astrocytic signal time courses.

Residual movement artifacts that involved detectable movement along the z-direction were visually detected from the extracted temporal traces as events of both correlated and anti-correlated changes of fluorescence across a majority of the FOV. These events were additionally inspected in the raw movies and blanked for further analyses. Mice for which such strong motion artifacts occurred regularly were not further used for experiments and analyses.

Behavioral monitoring post-processing

The behavioral video was used to extract several behavioral features. The correlation between subsequent frames was used to compute the movement from two sub-regions that were manually drawn around the mouth and the front paws. The measured metric (1 - correlation) was scaled by the maximum within each session. Pupil diameter could be quantified since the infrared laser light of the two-photon system exited the pupil, which in turn appeared bright in the behavioral camera video. The equivalent diameter was computed from the area of the pupil, which in turn was obtained from a simple segmentation of the pupil with standard image processing methods. Briefly, the brightest round object in the ROI covering the eye was extracted from the binarized image using the *regionprops()* function in MATLAB (MathWorks). Dark spots inside the segmented pupil due to reflections were filled and connections of the segmented pupil to the bright upper eyelid were removed by repeated binary erosion and dilation of the segmented pupil. Occasional winking events were manually detected from the extracted pupil diameter traces, confirmed by video inspection, and automatically replaced by values obtained via linear interpolation. The difference between illumination periodicity (from the imaging system, 30.88 Hz) and the recording rate (30 Hz) resulted in a beating pattern of 0.88 Hz that was also visible in the extracted pupil signal. A template filter based on the 0.88 Hz periodicity was used to remove this

bioRxiv preprint doi: https://doi.org/10.1101/2022.08.16.504030; this version posted August 17, 2022. The copyright holder for this preprint (which was not certified by peer review) is the author/funder, who has granted bioRxiv a license to display the preprint in perpetuity. It is made available under aCC-BY-NC 4.0 International license.

illumination-induced component from the extracted pupil diameter. For the analyses in Figs. 3,4 and 5, where the absolute values of the observed pupil diameter was not important for the analysis, the absolute pupil diameter was used. For analyses associated with Fig. 7, to allow for pooling of pupil diameter values across sessions, pupil diameters were normalized (z-score) for each behavioral session to account for variable lighting conditions.

Similarly, licking was quantified by classical segmentation methods that detected the presence of a bright and large object close to the lick spout (the tongue). The final output was binarized (licking vs. non-licking) based on a threshold of detected object size. The threshold for lick detection was adjusted manually for each session and for each mouse while inspecting the resulting segmentation together with the raw behavioral movies.

The absolute position of the mouse on the treadmill belt was computed using the run speed recorded with the rotary encoder as a relative position signal and the analog IR diode output, which increased when a stripe of reflective tape at the backside of the belt went past the diode, as an absolute position signal.

Modeling global astrocytic activity with dilated linear regression

To model global astrocytic activity as a function of other variables (*e.g.,* paw movement, pupil diameter or location), we used a dilated variant of linear temporal regression. Specifically, we averaged time points of the regressor around the to-be-regressed time point into bins that exponentially increased their width with the temporal distance from the current time point. Therefore, the first bin was 1 frame in width, the second 2 frames, the third 4 frames, the fourth 8 frames, and so on, resulting in an effective time window of ±17 s (±512 time points sampled at 30 Hz). This "dilated linear regression" is inspired by "dilated convolutions" used for signal processing and deep neuronal networks[83,84] and serves to reduce the number of regressors while providing a multi-scale representation of the regressor variable. Such a reduction of the number of regressors is necessary to avoid overfitting. Overfitting is a problem when regressing global astrocytic signals, which provide – due to their slowly changing nature – only relatively few statistically independent data points even for longer recordings.

The vector of such dilated regressors was used to linearly regress the observed global astrocytic activity with the *glmfit()* function in MATLAB. Performance was evaluated on 5-fold cross-validated subsets within each recorded session to exclude overfitting. Performance was measured using the correlation between predicted and true signals across the 5 cross-validated segments of the entire session.

Modeling global astrocytic activity with a linear differential equation

A standard leaky-integrator differential equation of the form

$$\tau \frac{dA(t)}{dt} = -A(t) + I(t) \qquad (1)$$

was implemented, with the integration time constant τ, the astrocytic activity $A(t)$ and the regressor input $I(t)$. Fitting was performed by grid search of the parameter τ and by evaluating the correlation of the recorded signal with the signal obtained by simulation of the differential equation. Since the correlation is not affected by the scaling of the two compared signals, a scaling factor of the input regressor $I(t)$ was not necessary. For the evaluation, the first time points until $t = 2\tau$ were excluded to avoid the influence of the initial conditions during the simulation of the differential equation.

bioRxiv preprint doi: https://doi.org/10.1101/2022.08.16.504030; this version posted August 17, 2022. The copyright holder for this preprint (which was not certified by peer review) is the author/funder, who has granted bioRxiv a license to display the preprint in perpetuity. It is made available under aCC-BY-NC 4.0 International license.

Self-supervised denoising of calcium movies

Two-photon calcium imaging movies are often dominated by shot noise. Due to the sensitivity of astrocytes to laser-induced heating[85], we limited the laser power in our experiments to moderate values, at the cost of a decreased signal-to-noise ratio. To enable complex analyses with single-pixel precision despite noisy pixel traces, we used recently developed algorithms for self-supervised denoising of imaging data based on deep networks[86,87], implemented in the Python scripts of DeepInterpolation[35]. This implementation uses the pixels of the 30 frames prior and after the current frame to denoise the pixels of the current frame. More precisely, the algorithm infers for each pixel the value that is most likely, based on its spatio-temporal surrounding pixels and based on the priors of the networks. To adapt the network priors from previously established neuronal recordings[35] to our astrocytic recordings, we retrained the deep network from scratch for each analyzed session with 10,000 frames of the recording and then ran the trained network on all imaging frames of the respective session. To enable the highest precision and to avoid (anti-)correlated movement artifacts through brain motion, we applied an algorithm for piecewise rigid motion correction on the denoised data[88]. While an entirely rigid motion correction algorithm corrects for most of the movement artifacts, the piecewise rigid motion correction also was able to correct small or nonlinear distortions that happened on faster timescales than the frame rate and required a denoised input.

Delay maps of astrocytic activity

We used the global astrocytic activity (average across the entire FOV) as a global reference to compute the average delay of each pixel's signal with respect to this global reference. To extract the average delay, we computed the correlation function between the reference signal and the pixel's time trace, which was extracted from the denoised movie (described above). The correlation function was normalized such that the zero-lag component was identical with Pearson's correlation coefficient. Next, the correlation function was smoothed with a 0.5-s window filter and the delay determined by taking the maximum of the correlation function in a -10 … +10 s window around the zero-lag time point. This procedure was repeated for each pixel, resulting in a map of delays. Such a map was computed for each 140-s segment in a session and per-segment maps were combined to a session-map using weighted averaging, with the mean astrocytic activation (ΔF/F) of the entire FOV within the respective segment as the weight used for averaging. This procedure, comprising retraining and application of the self-supervised denoising network and the computation of delay maps, was applied to a total of 12 selected sessions that fulfilled the following criteria: (1) A sufficient amount of global astrocytic activity. For example, sessions with mice that barely moved during the sessions did not exhibit sufficient global astrocytic dynamics for a meaningful analysis. (2) Clearly visible astrocytic somata. In some sessions, especially when the recording FOV was constrained by simultaneous neuronal imaging in the pyramidal layer but also in other recordings with suboptimal imaging conditions, only gliapil but no clearly detectable cell bodies of astrocytes could be identified, making those recordings less useful for analyses comparing calcium signals in cell bodies vs. distal processes.

Identification of centripetally propagating vs. non-propagating calcium events

To extract FOV-wide temporal delay components, the delay map was smoothed with a shape-preserving 2D median filter (filter size 6 µm; Fig. 7a) and then binned by rounding the delay to integer values (…, -2 s, -1 s, 0 s, +1 s, +2 s, …). Pixels with

bioRxiv preprint doi: https://doi.org/10.1101/2022.08.16.504030; this version posted August 17, 2022. The copyright holder for this preprint (which was not certified by peer review) is the author/funder, who has granted bioRxiv a license to display the preprint in perpetuity. It is made available under aCC-BY-NC 4.0 International license.

the respective delays across the entire FOV (Fig. 7b) were used to extract the mean time trace from the denoised movie, and this time trace was used to compute ΔF/F (Fig. 7c). A 25 pixel-wide boundary of the FOV was discarded to prevent the contamination by lateral movement artifacts that cannot be corrected at image boundaries. In addition, pixels that contained identified interneurons through ectopic GFAP-driven expression of GCaMP6s were excluded for each FOV using a manually drawn blanking mask.

The temporal delay components (one time trace each for -2 s, -1 s, 0 s, +1 s, etc. pixels) were extracted as raw fluorescence traces and then normalized as ΔF/F values (F_0 defined as 20% quantile across the session for the respective delay component) to enable a comparison between normalized traces. The average across these traces was used to identify candidate events using the *findpeaks()* function in MATLAB. Since an average across delay components was used as a reference to detect events, it is likely that some gliapil-only events that did not propagate into the soma were not identified as events. The distribution of centripetally propagating and non-propagating events in Fig. 7d is therefore not representative but biased towards events that are also visible in processes closer to the soma. All candidate events were visually inspected and corrected. Typical events are shown in Fig. 7e, and other more complex events, which were still considered to be a single event for our analyses, are shown in Fig. S11. The beginning and end of events was estimated as the trough preceding or following an event peak, again proofed by visual inspection. For each event, the mean value of each delay component was extracted, and a linear fit ($y = a \cdot x + b$) computed, with the extracted mean as y-values and the delay in seconds as x-values (Fig. 7c, inset). The fit parameter a was normalized by b, the fitted value of y at zero-lag $x = 0$ s, resulting in the "propagation slope" as used throughout the Results section. This normalization has the side effect that errors due to division by small values of b for very small events can result in potentially erroneous large positive or negative slopes; however, at the same time it ensures that the propagation of small-amplitude events is equally considered compared to large-amplitude events. The fit was improved by using the number of FOV pixels that contributed to each delayed trace as fit weights.

To define putative astrocytic domains for single-cell analysis of delayed traces (Fig. S13), we manually seeded cell centers based on cell bodies. This analysis could only be performed for sessions in which astrocytic cell bodies could be clearly identified and distinguished from each other and from other structures like end-feet (n = 8 sessions). A watershed algorithm custom-written in MATLAB was used to simultaneously and iteratively expand the domains of all seed points using binary dilation until the domains encountered either the boundary of another domain or reached a distance of $\geqslant$35 µm from the seed point.

Statistics

Only non-parametric, two-sided tests were used (Mann-Whitney rank sum test and Wilcoxon signed-rank test for unpaired and paired conditions, respectively), and no corrections for multiple testing were performed. Box plots used standard settings in MATLAB, with the central line at the median of the distribution, the box at the 25th and 75th percentiles and the whiskers at extreme values excluding outliers.

bioRxiv preprint doi: https://doi.org/10.1101/2022.08.16.504030; this version posted August 17, 2022. The copyright holder for this preprint (which was not certified by peer review) is the author/funder, who has granted bioRxiv a license to display the preprint in perpetuity. It is made available under aCC-BY-NC 4.0 International license.

Acknowledgements

This work was support by grants to F.H. from the Swiss National Science Foundation (project grant 310030B_170269 and Sinergia grant CRSII5_180316 to F.H.), the European Research Council (ERC Advanced Grant BRAINCOMPATH, project 670757), and the NIH Brain Initiative (grant U01NS115585), and by grants to C.M.L. and P.R. (Forschungskredit grants from the University of Zurich, projects K-41220-04 and K-41220-06-01). We thank the group of Anna-Sophia Wahl for sharing their experience with the behavioral setup, and Stefan Giger, Martin Wieckhorst and Hansjörg Kasper for help and assistance with its construction. We thank Denise Becker, Antoine Adamantidis and Bruno Weber for feedback on the manuscript, and all members of the Helmchen Lab for critical input.

Contributions

P.R. conceived the study, established the methodology, carried out experiments, performed analyses, and wrote the paper; C.M.L. contributed to experiments and to the conceptualization of results; F.H. conceived the study, contributed to analyses, and wrote the paper.

Data availability

Example raw data of astrocytic calcium recordings together with Matlab and Python programs to compute delay maps as shown in Fig. 6 will be made available on Github upon publication of the manuscript. All other processed data used in the manuscript will be available from the corresponding author upon request.

Code availability

Example programs written in Matlab and Python to compute delay maps as shown in Fig. 6 from raw astrocytic calcium recordings will be made available on Github upon publication of the manuscript under https://github.com/HelmchenLabSoftware/Centripetal_propagation_astrocytes. All other custom code used for analyses described in the manuscript will be available from the corresponding author upon request.

Competing interests

The authors declare no competing interests.

bioRxiv preprint doi: https://doi.org/10.1101/2022.08.16.504030; this version posted August 17, 2022. The copyright holder for this preprint (which was not certified by peer review) is the author/funder, who has granted bioRxiv a license to display the preprint in perpetuity. It is made available under aCC-BY-NC 4.0 International license.

References

1. Ventura, R. & Harris, K. M. Three-Dimensional Relationships between Hippocampal Synapses and Astrocytes. J. Neurosci. 19, 6897–6906 (1999).
2. Araque, A., Parpura, V., Sanzgiri, R. P. & Haydon, P. G. Tripartite synapses: glia, the unacknowledged partner. Trends Neurosci. 22, 208–215 (1999).
3. Kastanenka, K. V. et al. A roadmap to integrate astrocytes into Systems Neuroscience. Glia 68, 5–26 (2020).
4. Kofuji, P. & Araque, A. Astrocytes and Behavior. Annu. Rev. Neurosci. 44, null (2021).
5. Curreli, S., Bonato, J., Romanzi, S., Panzeri, S. & Fellin, T. Complementary encoding of spatial information in hippocampal astrocytes. PLOS Biol. 20, e3001530 (2022).
6. Doron, A. et al. Hippocampal Astrocytes Encode Reward Location (2021). Preprint at https://doi.org/10.1101/2021.07.07.451434.
7. Schummers, J., Yu, H. & Sur, M. Tuned responses of astrocytes and their influence on hemodynamic signals in the visual cortex. Science 320, 1638–1643 (2008).
8. Slezak, M. et al. Distinct Mechanisms for Visual and Motor-Related Astrocyte Responses in Mouse Visual Cortex. Curr. Biol. 29, 3120-3127.e5 (2019).
9. Semyanov, A., Henneberger, C. & Agarwal, A. Making sense of astrocytic calcium signals — from acquisition to interpretation. Nat. Rev. Neurosci. 21, 551–564 (2020).
10. Stobart, J. L. et al. Cortical Circuit Activity Evokes Rapid Astrocyte Calcium Signals on a Similar Timescale to Neurons. Neuron 98, 726-735.e4 (2018).
11. Bindocci, E. et al. Three-dimensional Ca2+ imaging advances understanding of astrocyte biology. Science 356, (2017).
12. Kofuji, P. & Araque, A. G-Protein-Coupled Receptors in Astrocyte-Neuron Communication. Neuroscience 456, 71–84 (2021).
13. Wahis, J. & Holt, M. G. Astrocytes, Noradrenaline, α1-Adrenoreceptors, and Neuromodulation: Evidence and Unanswered Questions. Front. Cell. Neurosci. 15, (2021).
14. Musall, S., Kaufman, M. T., Juavinett, A. L., Gluf, S. & Churchland, A. K. Single-trial neural dynamics are dominated by richly varied movements. Nat. Neurosci. 22, 1677–1686 (2019).
15. Stringer, C. et al. Spontaneous behaviors drive multidimensional, brainwide activity. Science 364, (2019).
16. Ding, F. et al. α1-Adrenergic receptors mediate coordinated Ca2+ signaling of cortical astrocytes in awake, behaving mice. Cell Calcium 54, 387–394 (2013).
17. Paukert, M. et al. Norepinephrine controls astroglial responsiveness to local circuit activity. Neuron 82, 1263–1270 (2014).
18. Dombeck, D. A., Khabbaz, A. N., Collman, F., Adelman, T. L. & Tank, D. W. Imaging large scale neural activity with cellular resolution in awake mobile mice. Neuron 56, 43–57 (2007).
19. Merten, K., Folk, R. W., Duarte, D. & Nimmerjahn, A. Astrocytes encode complex behaviorally relevant information (2021). Preprint at https://doi.org/10.1101/2021.10.09.463784.
20. Nimmerjahn, A., Mukamel, E. A. & Schnitzer, M. J. Motor Behavior Activates Bergmann Glial Networks. Neuron 62, 400 (2009).
21. Armbruster, M. et al. Neuronal activity drives pathway-specific depolarization of peripheral astrocyte processes. Nat. Neurosci. 25, 607–616 (2022).
22. Wang, X. et al. Astrocytic Ca2+ signaling evoked by sensory stimulation in vivo. Nat. Neurosci. 9, 816–823 (2006).
23. Grewe, B. F., Voigt, F. F., Hoff, M. van 't & Helmchen, F. Fast two-layer two-photon imaging of neuronal cell populations using an electrically tunable lens. Biomed. Opt. Express 2, 2035–2046 (2011).
24. Refaeli, R. et al. Features of hippocampal astrocytic domains and their spatial relation to excitatory and inhibitory neurons. Glia 69, 2378–2390 (2021).
25. Dana, H. et al. Thy1-GCaMP6 transgenic mice for neuronal population imaging in vivo. PloS One 9, e108697 (2014).
26. Rupprecht, P. et al. A database and deep learning toolbox for noise-optimized, generalized spike inference from calcium imaging. Nat. Neurosci. 24, 1324–1337 (2021).
27. Reimer, J. et al. Pupil fluctuations track rapid changes in adrenergic and cholinergic activity in cortex. Nat. Commun. 7, 13289 (2016).
28. Larsen, R. S. & Waters, J. Neuromodulatory Correlates of Pupil Dilation. Front. Neural Circuits 12, 21 (2018).
29. Privitera, M. et al. A complete pupillometry toolbox for real-time monitoring of locus coeruleus activity in rodents. Nat. Protoc. 15, 2301–2320 (2020).
30. Yang, W. et al. Anesthetics fragment hippocampal network activity, alter spine dynamics, and affect memory consolidation. PLOS Biol. 19, e3001146 (2021).
31. Thrane, A. S. et al. General anesthesia selectively disrupts astrocyte calcium signaling in the awake mouse cortex. Proc. Natl. Acad. Sci. U. S. A. 109, 18974–18979 (2012).
32. Bojarskaite, L. et al. Astrocytic Ca2+ signaling is reduced during sleep and is involved in the regulation of slow wave sleep. Nat. Comm. 11, 3240 (2020).
33. Bekar, L. K., He, W. & Nedergaard, M. Locus coeruleus alpha-adrenergic-mediated activation of cortical astrocytes in vivo. Cereb. Cortex N. Y. N 1991 18, 2789–2795 (2008).

bioRxiv preprint doi: https://doi.org/10.1101/2022.08.16.504030; this version posted August 17, 2022. The copyright holder for this preprint (which was not certified by peer review) is the author/funder, who has granted bioRxiv a license to display the preprint in perpetuity. It is made available under aCC-BY-NC 4.0 International license.

34. Srinivasan, R. et al. Ca2+ signaling in astrocytes from Ip3r2−/− mice in brain slices and during startle responses in vivo. Nat. Neurosci. 18, 708–717 (2015).
35. Lecoq, J. et al. Removing independent noise in systems neuroscience data using DeepInterpolation. Nat. Methods 18, 1401–1408 (2021).
36. King, C. M. et al. Local Resting Ca2+ Controls the Scale of Astroglial Ca2+ Signals. Cell Rep. 30, 3466-3477.e4 (2020).
37. Sonoda, K., Matsui, T., Bito, H. & Ohki, K. Astrocytes in the mouse visual cortex reliably respond to visual stimulation. Biochem. Biophys. Res. Commun. 505, 1216–1222 (2018).
38. Oe, Y. et al. Distinct temporal integration of noradrenaline signaling by astrocytic second messengers during vigilance. Nat. Commun. 11, 471 (2020).
39. Kaufman, A. M., Geiller, T. & Losonczy, A. A Role for the Locus Coeruleus in Hippocampal CA1 Place Cell Reorganization during Spatial Reward Learning. Neuron 105, 1018-1026.e4 (2020).
40. Asada, A. et al. Subtle modulation of ongoing calcium dynamics in astrocytic microdomains by sensory inputs. Physiol. Rep. 3, e12454 (2015).
41. Rungta, R. L. et al. Ca2+ transients in astrocyte fine processes occur via Ca2+ influx in the adult mouse hippocampus. Glia 64, 2093–2103 (2016).
42. Ma, Z., Stork, T., Bergles, D. E. & Freeman, M. R. Neuromodulators signal through astrocytes to alter neural circuit activity and behaviour. Nature 539, 428–432 (2016).
43. Mu, Y. et al. Glia Accumulate Evidence that Actions Are Futile and Suppress Unsuccessful Behavior. Cell 178, 27-43.e19 (2019).
44. Lee, C. R. & Margolis, D. J. Pupil Dynamics Reflect Behavioral Choice and Learning in a Go/NoGo Tactile Decision-Making Task in Mice. Front. Behav. Neurosci. 10, (2016).
45. Reimer, J. et al. Pupil fluctuations track fast switching of cortical states during quiet wakefulness. Neuron 84, 355–362 (2014).
46. Gray, S. R., Ye, L., Ye, J. Y. & Paukert, M. Noradrenergic terminal short-term potentiation enables modality-selective integration of sensory input and vigilance state. Sci. Adv. 7, eabk1378 (2021).
47. McCormick, D. A., Nestvogel, D. B. & He, B. J. Neuromodulation of Brain State and Behavior. Annu. Rev. Neurosci. 43, 391–415 (2020).
48. Musall, S., Urai, A. E., Sussillo, D. & Churchland, A. K. Harnessing behavioral diversity to understand neural computations for cognition. Curr. Opin. Neurobiol. 58, 229–238 (2019).
49. Ashwood, Z. C. et al. Mice alternate between discrete strategies during perceptual decision-making. Nat. Neurosci. 25, 201–212 (2022).
50. Gilad, A., Gallero-Salas, Y., Groos, D. & Helmchen, F. Behavioral Strategy Determines Frontal or Posterior Location of Short-Term Memory in Neocortex. Neuron 99, 814-828.e7 (2018).
51. Agarwal, A. et al. Transient Opening of the Mitochondrial Permeability Transition Pore Induces Microdomain Calcium Transients in Astrocyte Processes. Neuron 93, 587-605.e7 (2017).
52. Bjørnstad, D. M. et al. Begonia—A Two-Photon Imaging Analysis Pipeline for Astrocytic Ca2+ Signals. Front. Cell. Neurosci. 15, (2021).
53. Wang, Y. et al. Accurate quantification of astrocyte and neurotransmitter fluorescence dynamics for single-cell and population-level physiology. Nat. Neurosci. 22, 1936–1944 (2019).
54. Georgiou, L., Echeverría, A., Georgiou, A. & Kuhn, B. Ca+ activity maps of astrocytes tagged by axoastrocytic AAV transfer. Sci. Adv. 8, eabe5371 (2022).
55. Di Castro, M. A. et al. Local Ca2+ detection and modulation of synaptic release by astrocytes. Nat. Neurosci. 14, 1276–1284 (2011).
56. Araque, A. et al. Gliotransmitters Travel in Time and Space. Neuron 81, 728–739 (2014).
57. Bittner, K. C., Milstein, A. D., Grienberger, C., Romani, S. & Magee, J. C. Behavioral time scale synaptic plasticity underlies CA1 place fields. Science 357, 1033–1036 (2017).
58. Santello, M., Toni, N. & Volterra, A. Astrocyte function from information processing to cognition and cognitive impairment. Nat. Neurosci. 22, 154–166 (2019).
59. Henneberger, C., Papouin, T., Oliet, S. H. R. & Rusakov, D. A. Long-term potentiation depends on release of D-serine from astrocytes. Nature 463, 232–236 (2010).
60. Papouin, T., Dunphy, J. M., Tolman, M., Dineley, K. T. & Haydon, P. G. Septal Cholinergic Neuromodulation Tunes the Astrocyte-Dependent Gating of Hippocampal NMDA Receptors to Wakefulness. Neuron 94, 840-854.e7 (2017).
61. Shigetomi, E., Jackson-Weaver, O., Huckstepp, R. T., O'Dell, T. J. & Khakh, B. S. TRPA1 channels are regulators of astrocyte basal calcium levels and long-term potentiation via constitutive D-serine release. J. Neurosci. Off. J. Soc. Neurosci. 33, 10143–10153 (2013).
62. Adamsky, A. et al. Astrocytic Activation Generates De Novo Neuronal Potentiation and Memory Enhancement. Cell 174, 59-71.e14 (2018).
63. Hösli, L. et al. Decoupling astrocytes in adult mice impairs synaptic plasticity and spatial learning. Cell Rep. 38, (2022).
64. Navarrete, M. et al. Astrocytes Mediate In Vivo Cholinergic-Induced Synaptic Plasticity. PLOS Biol. 10, e1001259 (2012).
65. Takata, N. et al. Astrocyte Calcium Signaling Transforms Cholinergic Modulation to Cortical Plasticity In Vivo. J. Neurosci. 31, 18155–18165 (2011).
66. Zhang, K. et al. Fear learning induces α7-nicotinic acetylcholine receptor-mediated astrocytic responsiveness that is required for memory persistence. Nat. Neurosci. 24, 1686–1698 (2021).
67. Kang, J., Jiang, L., Goldman, S. A. & Nedergaard, M. Astrocyte-mediated potentiation of inhibitory synaptic transmission. Nat. Neurosci. 1, 683–692 (1998).

bioRxiv preprint doi: https://doi.org/10.1101/2022.08.16.504030; this version posted August 17, 2022. The copyright holder for this preprint (which was not certified by peer review) is the author/funder, who has granted bioRxiv a license to display the preprint in perpetuity. It is made available under aCC-BY-NC 4.0 International license.

68. Bezzi, P. et al. Prostaglandins stimulate calcium-dependent glutamate release in astrocytes. Nature 391, 281–285 (1998).
69. Parpura, V. et al. Glutamate-mediated astrocyte-neuron signalling. Nature 369, 744–747 (1994).
70. Covelo, A. & Araque, A. Neuronal activity determines distinct gliotransmitter release from a single astrocyte. eLife 7, e32237 (2018).
71. Bohmbach, K. et al. An astrocytic signaling loop for frequency-dependent control of dendritic integration and spatial learning (2021). Preprint at https://doi.org/10.1101/2021.11.05.467400.
72. Coggan, J. S. et al. Norepinephrine stimulates glycogenolysis in astrocytes to fuel neurons with lactate. PLOS Comput. Biol. 14, e1006392 (2018).
73. Magistretti, P. J. & Allaman, I. Lactate in the brain: from metabolic end-product to signalling molecule. Nat. Rev. Neurosci. 19, 235–249 (2018).
74. Savtchouk, I. & Volterra, A. Gliotransmission: Beyond Black-and-White. J. Neurosci. 38, 14–25 (2018).
75. Dombeck, D. A., Harvey, C. D., Tian, L., Looger, L. L. & Tank, D. W. Functional imaging of hippocampal place cells at cellular resolution during virtual navigation. Nat. Neurosci. 13, 1433–1440 (2010).
76. Pilz, G.-A. et al. Functional Imaging of Dentate Granule Cells in the Adult Mouse Hippocampus. J. Neurosci. 36, 7407–7414 (2016).
77. Schoenfeld, G., Carta, S., Rupprecht, P., Ayaz, A. & Helmchen, F. In Vivo Calcium Imaging of CA3 Pyramidal Neuron Populations in Adult Mouse Hippocampus. eNeuro 8, (2021).
78. Chen, J. L., Voigt, F. F., Javadzadeh, M., Krueppel, R. & Helmchen, F. Long-range population dynamics of anatomically defined neocortical networks. eLife 5, e14679 (2016).
79. Urai, A. E. et al. Citric Acid Water as an Alternative to Water Restriction for High-Yield Mouse Behavior. eNeuro 8, (2021).
80. Dubbs, A., Guevara, J. & Yuste, R. moco: Fast Motion Correction for Calcium Imaging. Front. Neuroinformatics 10, (2016).
81. Rupprecht, P. & Friedrich, R. W. Precise Synaptic Balance in the Zebrafish Homolog of Olfactory Cortex. *Neuron* **100**, 669-683.e5 (2018).
82. Junek, S., Chen, T.-W., Alevra, M. & Schild, D. Activity Correlation Imaging: Visualizing Function and Structure of Neuronal Populations. *Biophys. J.* **96**, 3801–3809 (2009).
83. Holschneider, M., Kronland-Martinet, R., Morlet, J. & Tchamitchian, Ph. *A Real-Time Algorithm for Signal Analysis with the Help of the Wavelet Transform*. 286 (1989).
84. Oord, A. van den *et al.* WaveNet: A Generative Model for Raw Audio. *ArXiv160903499 Cs* (2016). Preprint at https://doi.org/10.48550/arXiv.1609.03499.
85. Schmidt, E. & Oheim, M. Infrared Excitation Induces Heating and Calcium Microdomain Hyperactivity in Cortical Astrocytes. *Biophys. J.* **119**, 2153–2165 (2020).
86. Batson, J. & Royer, L. Noise2Self: Blind Denoising by Self-Supervision. in *Proceedings of the 36th International Conference on Machine Learning* 524–533 (PMLR, 2019).
87. Krull, A., Buchholz, T.-O. & Jug, F. Noise2Void - Learning Denoising from Single Noisy Images. *ArXiv181110980 Cs* (2019).
88. Pnevmatikakis, E. A. & Giovannucci, A. NoRMCorre: An online algorithm for piecewise rigid motion correction of calcium imaging data. *J. Neurosci. Methods* **291**, 83–94 (2017).

bioRxiv preprint doi: https://doi.org/10.1101/2022.08.16.504030; this version posted August 17, 2022. The copyright holder for this preprint (which was not certified by peer review) is the author/funder, who has granted bioRxiv a license to display the preprint in perpetuity. It is made available under aCC-BY-NC 4.0 International license.

Supplementary figures

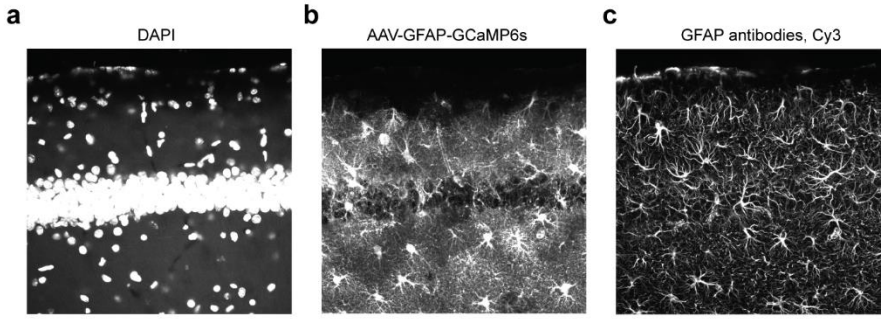

Figure S1 | Histology, all channels of Fig. 1d, shown separately in grayscale. a, nuclear stain DAPI. **b,** Virus-induced GCaMP6s expression in hippocampal astrocytes. **c,** GFAP-antibody staining of astrocytes. Maximum intensity projection across 12 µm. While antibodies tended to more heavily stain the distal processes of astrocytes, all astrocytes labeled with the GFAP antibody also exhibited expression with AAV-induced GCaMP6s.

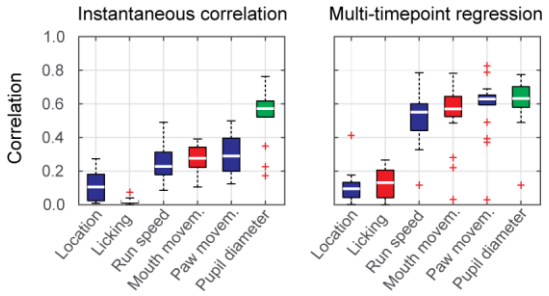

Figure S2 | Global astrocytic activity can be well explained by past behavior, mean neuronal spike rate or pupil diameter, continuation. Same analysis as in Fig. 3c,d but for a different set of animals, in which calcium imaging was performed in astrocytes only (thus lacking the predictions by neuronal ΔF/F and SR; 19 imaging sessions from 3 animals). Results are similar to the results for the 4 animals shown in Fig. 3c,d.

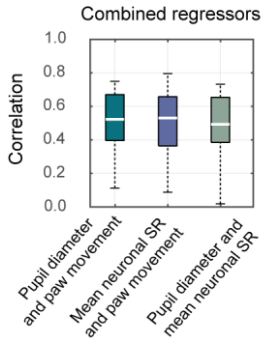

Figure S3 | Predictions of global astrocytic activity based on combined regressors. Using combined regressors (*e.g.,* pupil diameter and paw movement) instead of a single regressor (*e.g.,* only pupil diameter) did not improve predictions, as measured by correlation values (y-axis). This result is likely due to two effects. First, the auto-correlated astrocytic signal results in relatively few independent data points that result in overfitting when increasing the number of regressors and deterioration of cross-validated predictions. Second, distinct regressors result in highly similar predictions due to redundant signals (Fig. 3e,f), resulting in lack of strong improvements when combining regressors.

bioRxiv preprint doi: https://doi.org/10.1101/2022.08.16.504030; this version posted August 17, 2022. The copyright holder for this preprint (which was not certified by peer review) is the author/funder, who has granted bioRxiv a license to display the preprint in perpetuity. It is made available under aCC-BY-NC 4.0 International license.

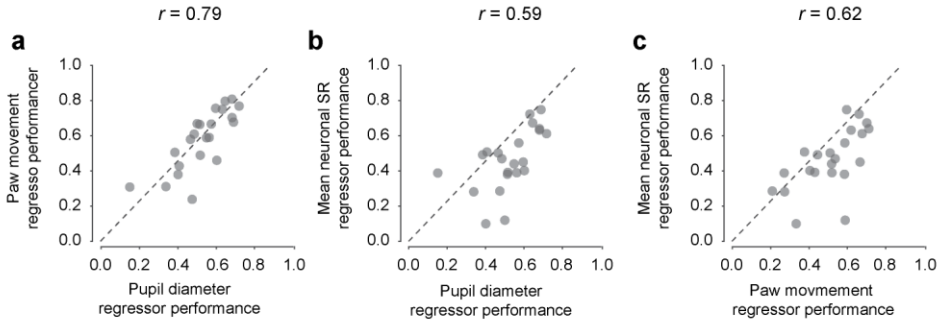

Figure S4 | Performance for different regressors across sessions is highly correlated. Extension of Fig. 3g. **a,** Performance of pupil diameter vs. paw movement as regressors. **b,** Performance of pupil diameter vs. mean neuronal spike rate (SR) as regressors. **c,** Performance of paw movement vs. mean neuronal spike rate as regressors. For all panels, a single data point represents the average performance of the cross-validated dilated linear regression averaged for an imaging session. Values (*r*) indicate the correlation between the two regressor's performances. The dashed lines represent the identity relationship.

bioRxiv preprint doi: https://doi.org/10.1101/2022.08.16.504030; this version posted August 17, 2022. The copyright holder for this preprint (which was not certified by peer review) is the author/funder, who has granted bioRxiv a license to display the preprint in perpetuity. It is made available under aCC-BY-NC 4.0 International license.

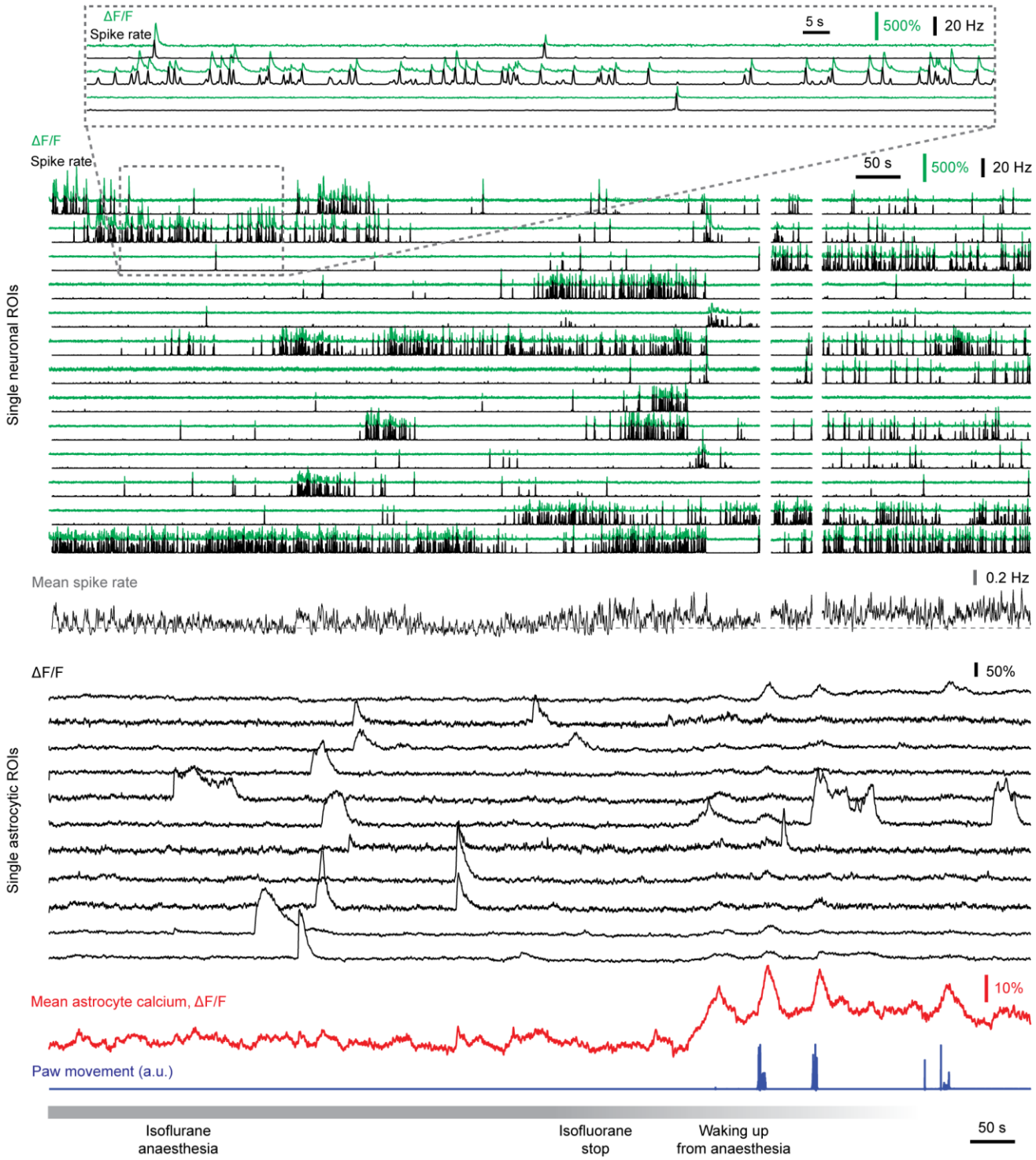

Figure S5 | Calcium imaging of astrocytes and pyramidal neurons in CA1 during isoflurane anesthesia. Examples of extracted neuronal ΔF/F traces (green) and associated deconvolved spike rates (black) are shown (see also zoom-in at the top). White blanked time points were discarded due to excessive movement of the brain during the waking-up. Example astrocytic ΔF/F traces (black) are shown below, highlighting uncoordinated local but no global events before the waking up. Waking up (bottom; 1.5% in the beginning, set to 0% at "isoflurane stop") is reflected by small and large paw movements (blue) and resulted in global astrocytic calcium signals (mean astrocytic calcium, red).

bioRxiv preprint doi: https://doi.org/10.1101/2022.08.16.504030; this version posted August 17, 2022. The copyright holder for this preprint (which was not certified by peer review) is the author/funder, who has granted bioRxiv a license to display the preprint in perpetuity. It is made available under aCC-BY-NC 4.0 International license.

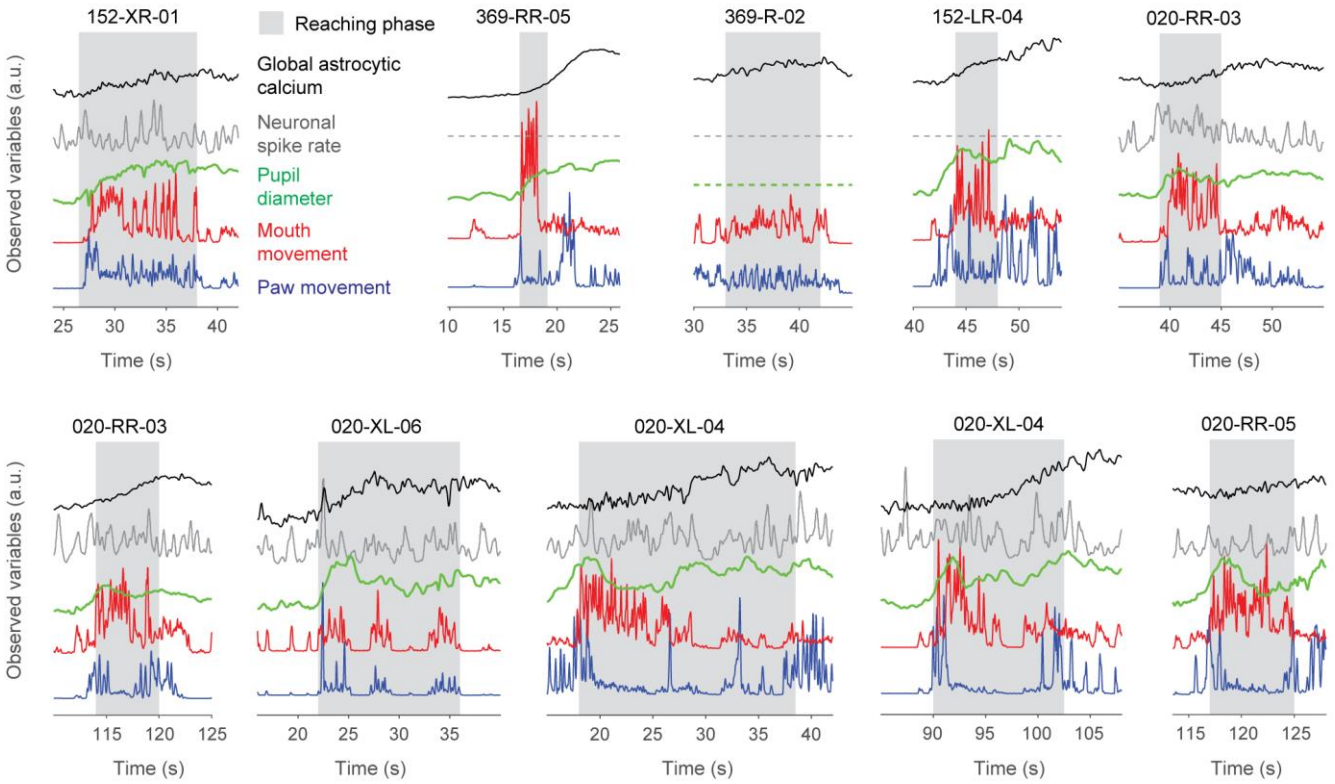

Figure S6 | Global astrocytic calcium increases during non-locomotor movements (reaching). Simultaneously recorded variables are color-coded and represented with dashed flat lines if no recordings were available. Panel titles indicate mouse ID (*e.g.,* 152-XR for the first panel) and the respective imaging session (*e.g.,* 01). The (manually defined) grasping phase is highlighted as gray background. Reaching, which resulted in paw movement close to the lick spout in proximity of the mouth, is usually visible as deflections of the "mouth movement" (red). All events in this figure are shown, together with the recorded variables and the behavioral video in Movie 5.

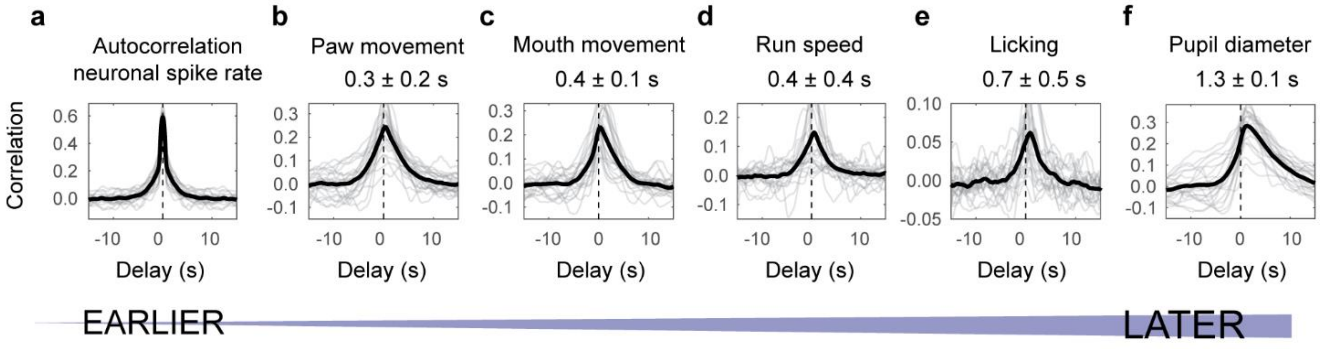

Figure S7 | Temporal sequence of behavioral variables with respect to mean neuronal spike rate. Analogous to Fig. 5 but using deconvolved neuronal spike rate instead of global astrocytic activity as the reference signal. A peak of the correlation function with positive lag indicates that neuronal spike rate peaked on average earlier than the inspected variable. Grey traces are correlation functions extracted from single sessions, black traces are averages across sessions. The delays indicated are median values ± standard error across sessions (n = 22 sessions across 4 animals).

bioRxiv preprint doi: https://doi.org/10.1101/2022.08.16.504030; this version posted August 17, 2022. The copyright holder for this preprint (which was not certified by peer review) is the author/funder, who has granted bioRxiv a license to display the preprint in perpetuity. It is made available under aCC-BY-NC 4.0 International license.

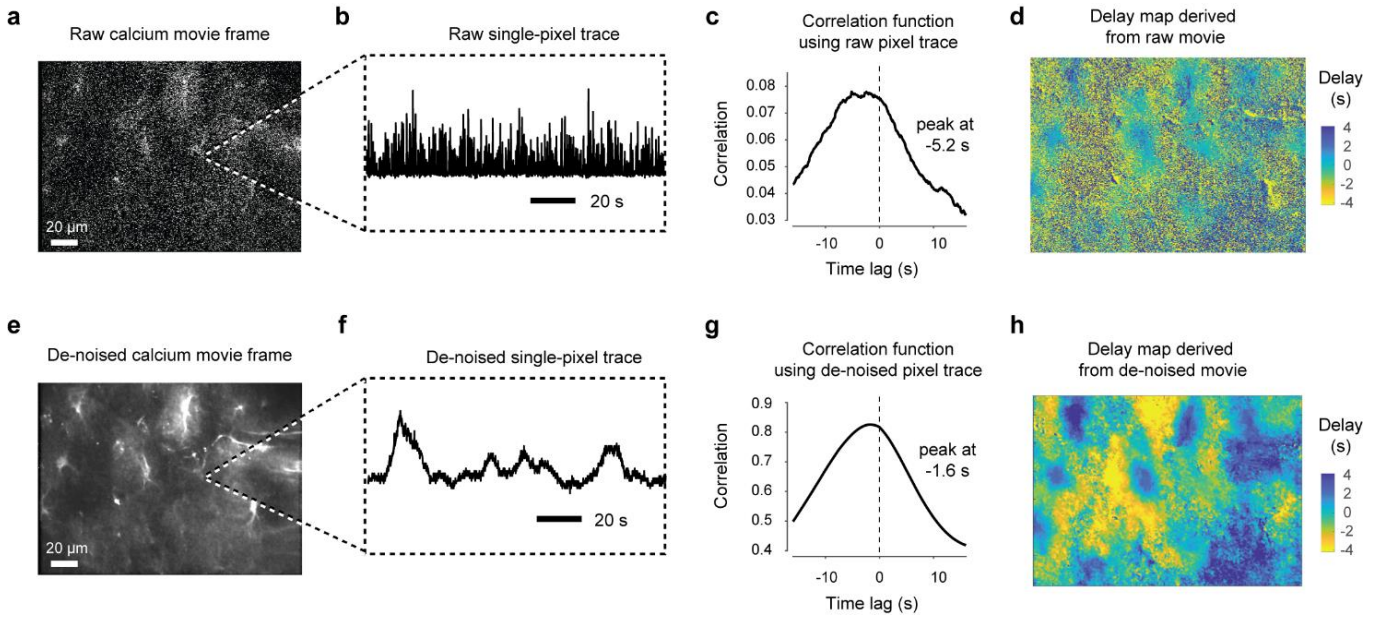

Figure S8 | Pixel-wise computation of delays is improved by self-supervised de-noising. The top row shows the results of the processing pipeline as described in Fig. 6e but without de-noising of the raw movie, the bottom row the results using the de-noised movie **a,** Single frame of the raw movie. **b,** Single-pixel trace extracted from the raw movie in (a). **c,** Correlation function computed from the pixel trace in (b) with the global astrocytic activity across the entire FOV. The peak of the correlation function is, in this case, detected at -5.2 s. **d,** Delays for all pixel traces, mapped onto the imaging FOV. **e-h,** Same as (a-d) but based on the de-noised movie. The resulting delay maps (h) are less noisy than in (d).

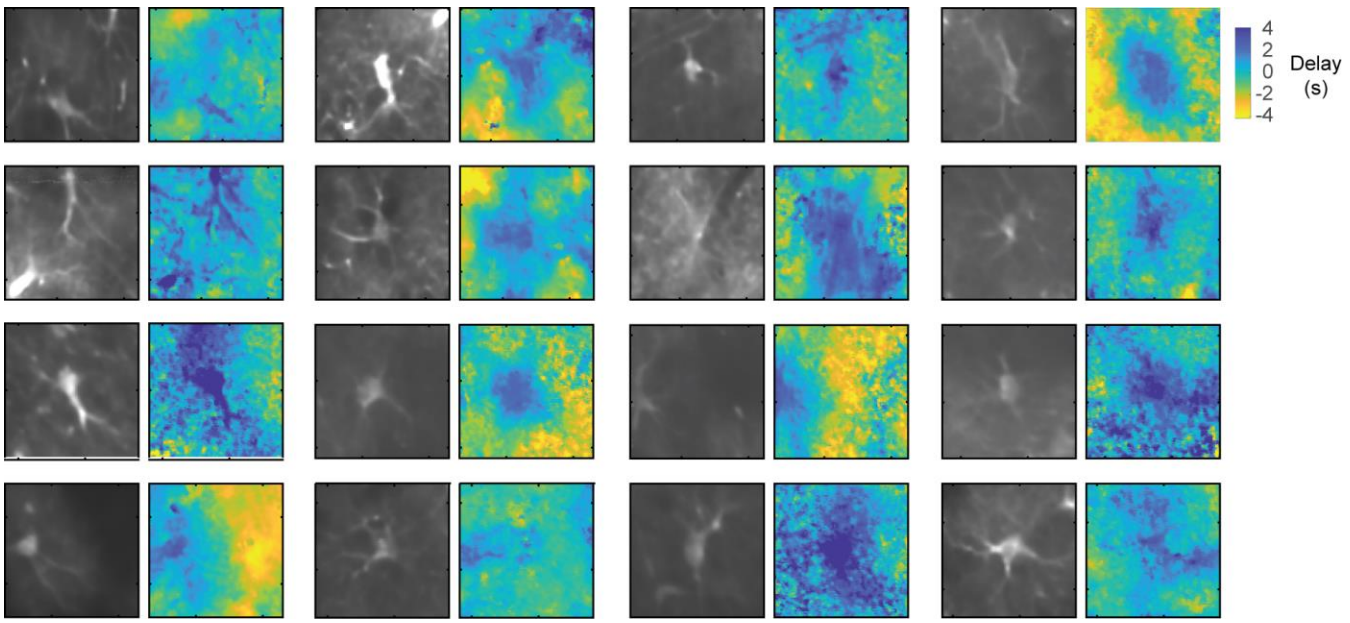

Figure S9 | Further examples of isolated astrocytes (fluorescence average, left) together with the local delay maps (right). Extension of Fig. 6h. The color code (as in Fig. 6) indicates propagation of activity from distal to somatic compartments on a timescale of seconds. The side length of each FOV excerpt is approximately 55 µm.

bioRxiv preprint doi: https://doi.org/10.1101/2022.08.16.504030; this version posted August 17, 2022. The copyright holder for this preprint (which was not certified by peer review) is the author/funder, who has granted bioRxiv a license to display the preprint in perpetuity. It is made available under aCC-BY-NC 4.0 International license.

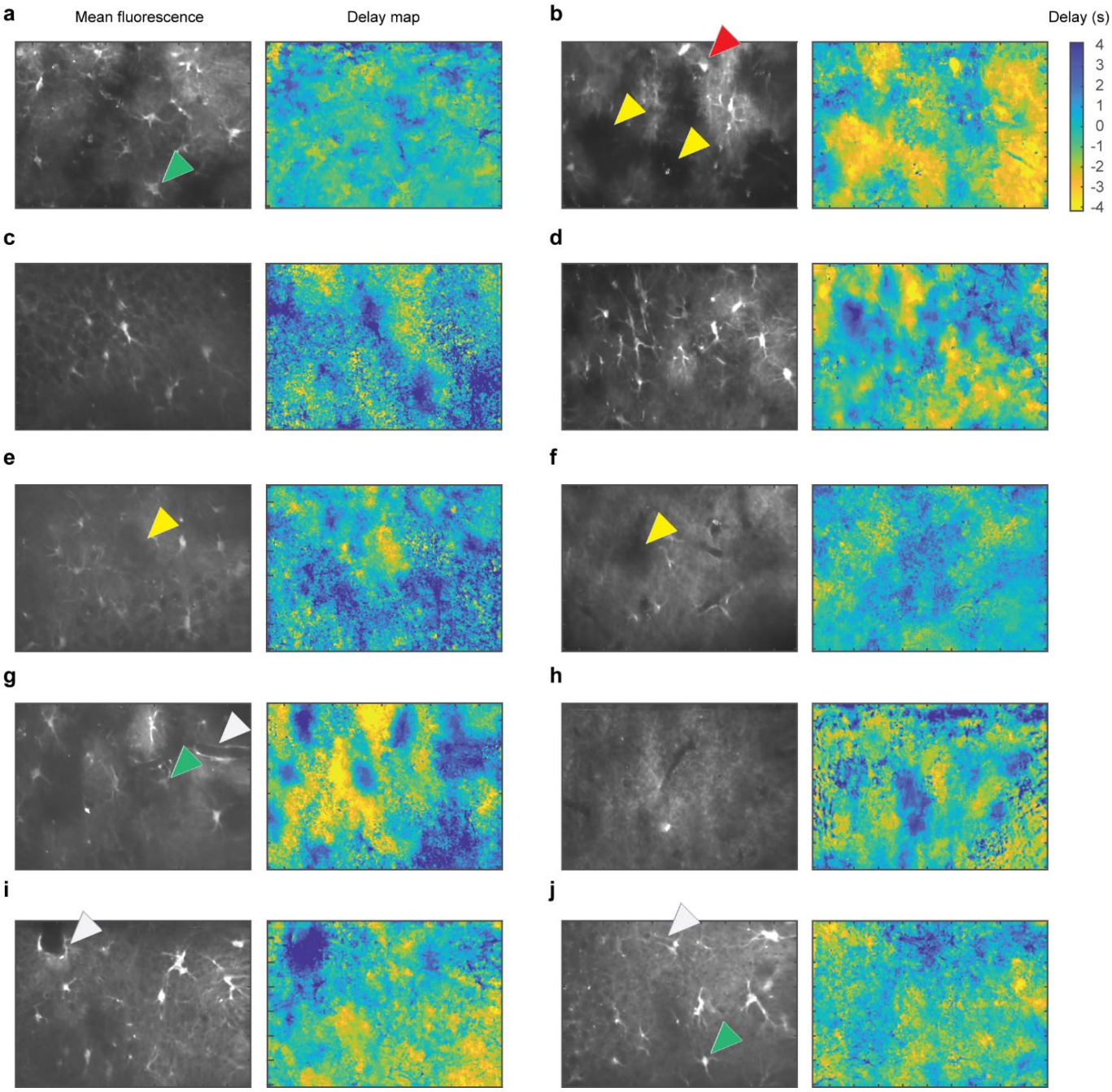

Figure S10 | Examples of delay maps. a-j, Maps of delays of astrocytic signal with respect to the global mean fluorescence, computed as described in Fig. 6 and Supplementary Fig. S8. Each delay map represents an entire imaging FOV (40x objective, 200 µm side length in x-direction). Yellow arrow heads highlight regions that are devoid of somata and thick processes, therefore mostly containing fine gliapil processes. Green arrow heads highlight astrocytic somata that are, unlike other soma examples shown in Fig. 6h and Fig. S9, not activated in a delayed manner with respect to the global mean activation. White arrow heads highlight astrocyte processes around blood vessels, exhibiting a very clear delayed activation with respect to the global mean activity. The red arrow head highlights an ectopically labeled interneuron; such interneuron pixels were blanked for the analysis in Fig. 7.

bioRxiv preprint doi: https://doi.org/10.1101/2022.08.16.504030; this version posted August 17, 2022. The copyright holder for this preprint (which was not certified by peer review) is the author/funder, who has granted bioRxiv a license to display the preprint in perpetuity. It is made available under aCC-BY-NC 4.0 International license.

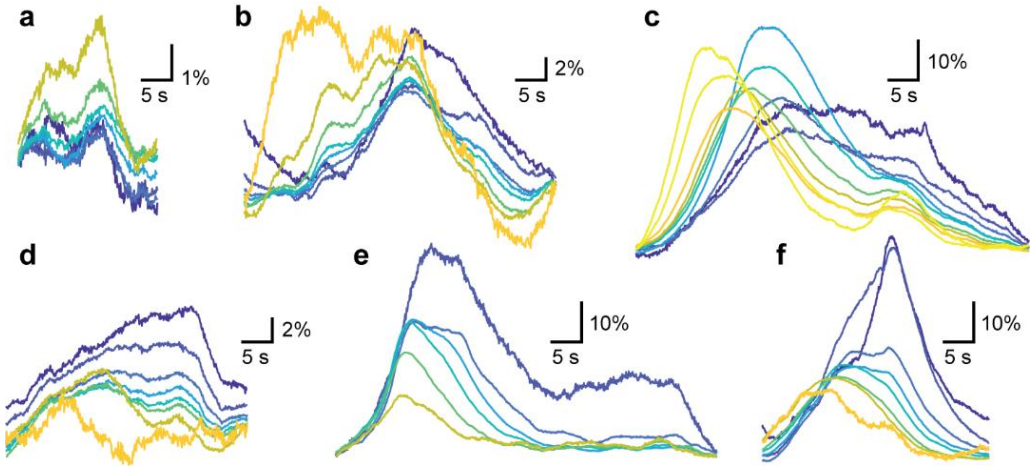

Figure S11 | Example events, extension of Fig. 7e. These examples highlight the diversity of astrocytic events that cannot always be well captured as single-phase events. Note the different vertical scale bars. The horizontal scale bars are identical across events. **a,** Example of a fading event (as defined in Fig. 7) that is barely visible except in the gliapil (yellow). **b,** Biphasic gliapil event. The first gliapil activation (yellow) does not result in centripetal propagation of calcium activity, but a second peak of gliapil activity manages to do so. **c,** Another example of biphasic gliapil activation. The first peak results in centripetal propagation, while the second gliapil peak is only weakly reflected by somatic calcium. **d,** Another example of biphasic gliapil activity. Slow somatic integration barely reflects the faster gliapil fluctuations. **e,** Example of very prominent centripetal propagation, resulting in longer-lasting activation of the somatic region. **f,** Similarly prominent centripetal propagation, resulting in a striking display of somatic calcium activity.

bioRxiv preprint doi: https://doi.org/10.1101/2022.08.16.504030; this version posted August 17, 2022. The copyright holder for this preprint (which was not certified by peer review) is the author/funder, who has granted bioRxiv a license to display the preprint in perpetuity. It is made available under aCC-BY-NC 4.0 International license.

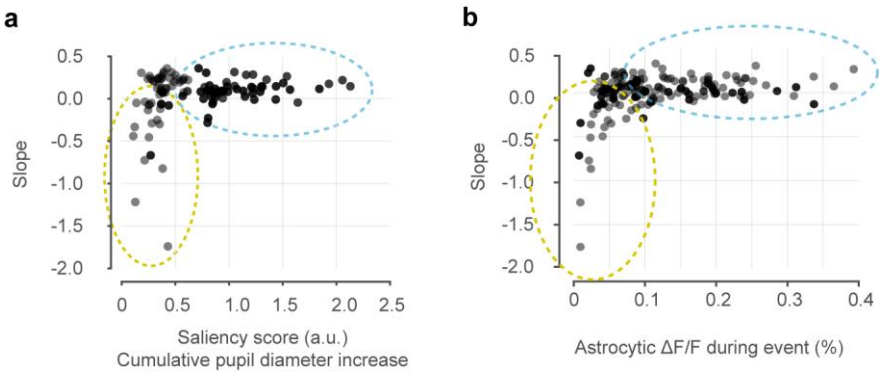

Figure S12 | Slope of astrocytic global events as a function of calcium event magnitude and of a 'saliency score'. Panels are analogous to panels Fig. 7d, but use the astrocytic mean ΔF/F value (a) or the saliency score (b) instead of pupil diameter as the dependent variable (x-axis). The saliency score is computed from the sum of the rectified derivative of the measured pupil diameter in the time window during the event, but shifted to the past by 2 seconds. The score therefore measures the amount of (positive) pupil change, instead of pupil diameter itself.

bioRxiv preprint doi: https://doi.org/10.1101/2022.08.16.504030; this version posted August 17, 2022. The copyright holder for this preprint (which was not certified by peer review) is the author/funder, who has granted bioRxiv a license to display the preprint in perpetuity. It is made available under aCC-BY-NC 4.0 International license.

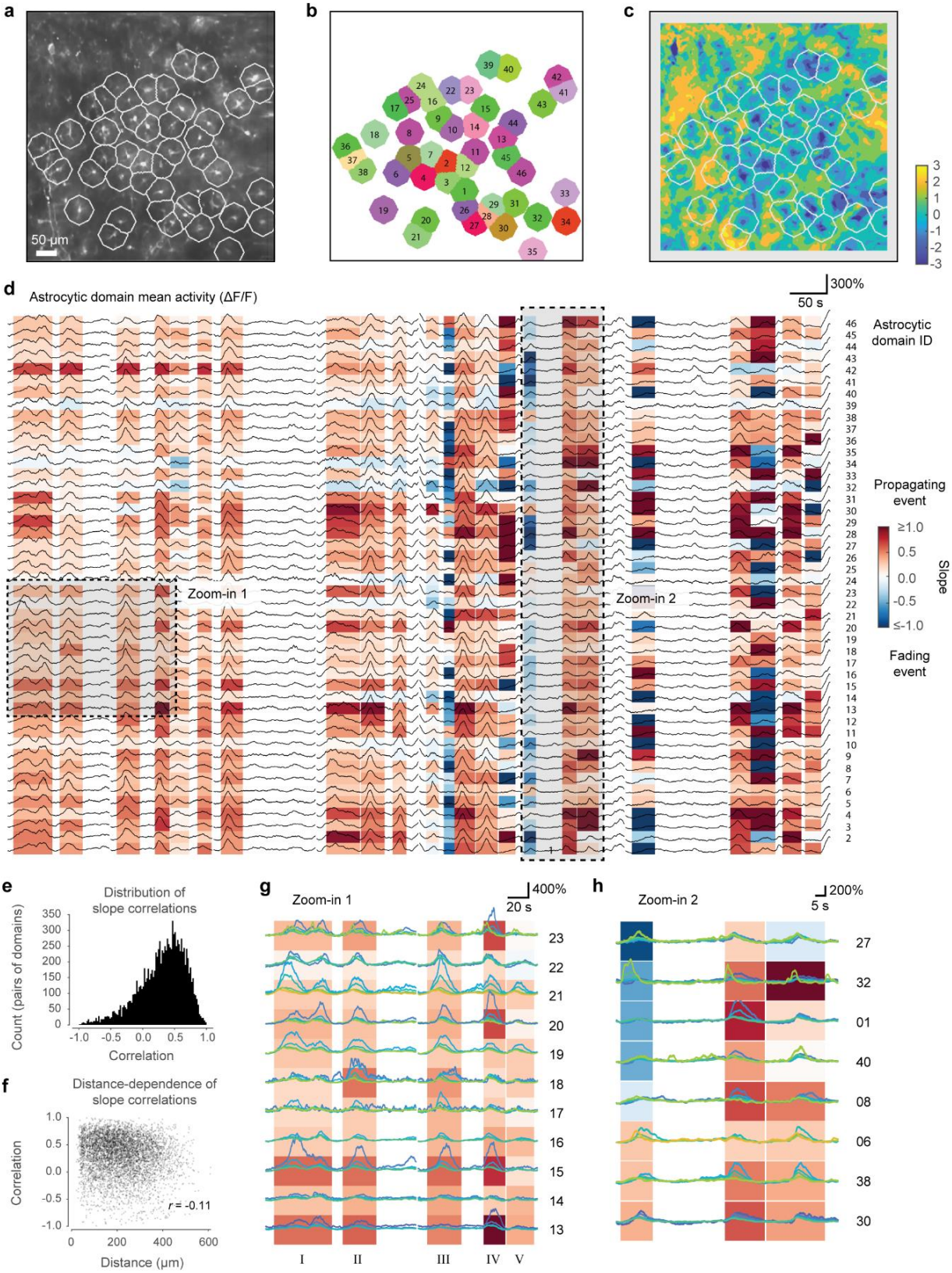

Figure S13 | Centripetal propagation can be variable across different putative single astrocytic domains. Manual seeding of the astrocyte cell body centroid with subsequent watershed segmentation was used to create putative astrocytic domains (cell

bioRxiv preprint doi: https://doi.org/10.1101/2022.08.16.504030; this version posted August 17, 2022. The copyright holder for this preprint (which was not certified by peer review) is the author/funder, who has granted bioRxiv a license to display the preprint in perpetuity. It is made available under aCC-BY-NC 4.0 International license.

bodies identified based on average fluorescence in **(a)**, segmented domains with ID numbers in **(a)**). For each domain, the delay map **(c)** was used to extract delayed traces as shown in Fig. 7a-c, and a slope was fitted for the delayed traces for each detected event and each astrocytic domain, as described in Fig. 7c. Positive slope (blue) indicates an event propagating into the somatic region of the respective domain, a negative slope (red) indicates a fading event **(d)**. Overlaid traces display the average activity in the respective domain. **e,** Similarity of slopes across events for pairs of astrocytic domains quantified as correlation. The distribution is centered on positive values, showing that most astrocytic domains follow the propagation/fading of the majority of other domains. **f,** Distance-dependence of the pair-wise correlations of propagation slopes from (e), indicating a weak decay of the correlation with distance. However, low correlations occur also at neighboring domains (distance approx. 20-50 µm), and high correlations at large distances. **g,** Centripetal propagation appears more prominent in some astrocytic domains for some events. Zoom-in #1 from (d) into a subset of events (event numbers in roman numerals below) and astrocytic domains (numbers at the right side). In addition, delayed traces are shown (color-coding as in Fig. 7; from yellow = distal processes, to blue = astrocytic soma). In some domains, the somatic trace is activated much more than for other domains (*e.g.,* domain 15) or for other events in other domains (*e.g.,* domain 18 for event II, domain 20 for event IV, and domain 23 for event IV). This observation indicates that the strength of somatic activation by centripetal propagation is variable across astrocytes. **h,** Zoom-in #2 from (d), manually re-ordered selection of traces (numbers to the right indicate the putative astrocytic domain). The first event is the event of interest for the purpose of this panel. While the event is globally dominated by fading calcium signals as seen in (d), calcium activity in some domains clearly reaches the somatic regions (astrocytic domain IDs 30, 38 and 6). This observation suggests that centripetal propagation is a cell-autonomous process that can occur in a subset of astrocytes.

bioRxiv preprint doi: https://doi.org/10.1101/2022.08.16.504030; this version posted August 17, 2022. The copyright holder for this preprint (which was not certified by peer review) is the author/funder, who has granted bioRxiv a license to display the preprint in perpetuity. It is made available under aCC-BY-NC 4.0 International license.

Movie captions

Movie 1 | Single-plane calcium imaging of hippocampal astrocytes *in vivo.* Calcium imaging of the calcium reporter GCaMP6s in the *stratum oriens* of hippocampal CA1 in a behaving mouse through an implanted cannula. The raw movie was denoised using a self-consistent denoising algorithm (DeepInterpolation, see Methods). For improved display of dim astrocytic processes, some of the brighter areas in the field of view are saturated. The field of view is 600 x 600 μm^2, the original frame rate 30.88 Hz (displayed at 10x speed).

Movie 2 | Triple-layer calcium imaging of hippocampal astrocytes *in vivo*. Calcium imaging of the calcium indicator GCaMP6s in three layers of hippocampal CA1 (left: *stratum oriens*, middle: *stratum pyramidale*, right: *stratum radiatum)* in a behaving mouse through an implanted cannula using a tunable lens for fast z-scanning. The raw movie was denoised using a self-consistent denoising algorithm (DeepInterpolation, see Methods). The original field of view for each plane is 200 x 200 μm^2, the original frame rate 10.29 Hz (displayed at 12x speed).

Movie 3 | Simultaneous monitoring of astrocytic and neuronal activity, pupil changes and body movement. The extracted traces are smoothed with a 5-point moving window and z-scored for clarity. The x-axis indicates time in seconds. The movie is displayed at real-time speed. Related to Figure 2.

Movie 4 | Examples of mouth movement without detectable effect on astrocytes. The extracted traces are smoothed with a 5-point moving window and z-scored for clarity. The x-axis indicates time in seconds. The movie is displayed at 2x speed. Related to Figure 3.

Movie 5 | Examples of front limb movements (reaching and grooming) and its effect on astrocytic activity. The extracted traces are smoothed with a 5-point moving window and z-scored for readability. The x-axis indicates time in seconds. The movie is displayed at 2x speed. Related to Figure S4.

Movie 6 | Self-consistent denoising of astrocytic calcium movies using DeepInterpolation. In the first part of the movie, the left version shows 140 s of a raw astrocytic calcium recording from hippocampal CA1 (*stratum oriens*). The right version shows the movie denoised using DeepInterpolation (see Methods). In the second part of the movie, the raw calcium movie is again shown together with the denoised version, but with the raw movie smoothed using a Gaussian filter (standard deviation 10 time points), resulting in smoothed time courses but visibly less efficient denoising compared to the self-consistent denoising method. Related to Figures 6 and S6.